North African soil dust and European pollution transport to America during the warm season: Hidden links shown by a passive tracer simulation

Gotzon Gangoiti,[1] Lucio Alonso,[1] Marino Navazo,[1] José Antonio García,[1] and Millán M. Millán[2]

Received 3 March 2005; revised 3 November 2005; accepted 25 January 2006; published 31 May 2006.

[1] A mesoscale atmospheric model coupled with a dispersion model is used to establish source-receptor relationships between the European-North African aerosol episodes observed over the Caribbean every year during summer and their main sources. The simulation period extends from 15 July to 16 August 1991, concurrent with the flight campaign of the European Project RECAPMA (Millán et al., 1997; Gangoiti et al., 2001). We now extend the simulations to reach the tropical Atlantic and the Caribbean, and we make use of the TOMS aerosol index data (Nimbus 7 satellite) to substantiate the simulations at the regional-to-continental scale. Our simulations, based on passive tracer release from selected source regions, show that emissions from southern Europe can either take a full-Atlantic shortcut to the American coasts or enter the Mediterranean basin eastward to turn back to America following a longer pathway: The emissions cross the southern Mediterranean coast to northern Africa, and then they are vented to the middle troposphere (2000–6000 m MSL), mixed within the Saharan air layer (SAL) and transported westward to the tropical Atlantic (TA) and America. Recirculations around the Atlas Mountains and perturbed conditions over the area modulate the export of the European tracer (and soil dust) into America. We found transit times of 11–12 days for the full Atlantic shortcut and 20–26 days for the longer pathway across northern Africa. Under the simulated conditions, southern Europe can contribute with more than the 50% of its emissions to America, while northern Europe shows longer transit times and less transport efficiency.

Citation: Gangoiti, G., L. Alonso, M. Navazo, J. A. García, and M. M. Millán (2006), North African soil dust and European pollution transport to America during the warm season: Hidden links shown by a passive tracer simulation, *J. Geophys. Res.*, *111*, D10109, doi:10.1029/2005JD005941.

1. Introduction

[2] Evidences of intercontinental transport (ICT) have accumulated over the past few years as new instrumental and processing techniques, including remote-sensing instruments onboard satellites, became available [*Herman et al.*, 1997; *Karyampudi et al.*, 1999; *Wilkening et al.*, 2000, *McKendry et al.*, 2001; *Wenig et al.*, 2003]. Experimental ground-based and flight campaigns have helped to document part of the long-range transport and dispersion mechanisms around the world. There is a need, however, to link observations unambiguously to source regions to understand cause-effect relationships. Model simulations can help to fill this gap and global models are currently used to feed the meteorological fields of dispersion models to simulate ICT [*Stohl et al.*, 2002; *Duncan and Bey*, 2004], usually with a low space-time resolution.

[3] Intercontinental transport (ICT) of aerosols, carbon monoxide, ozone and its precursors, and other persistent organic pollutants with spatial variations due to lifetimes ranging from a few days to several weeks, is initially driven by atmospheric daily processes and circulations at the regional scale. There is an increased need to understand the coupling between the various atmospheric motion scales implicated behind the observed transport of pollutants between continents. Many uncertainties still remain on how this type of transport affects the hydrological cycle, the radiation budget, the regional climate change impacts, and the air quality at very distant areas.

[4] Several aircraft campaigns have explored the continental outflow from North America (e.g., NARE [*Fehsenfeld et al.*, 1996]) and Asia (e.g., PEM-West B [*Hoell et al.*, 1997], TRACE-P [*Jacob et al.*, 2003]). European pollution also was identified in the 1980s as the main contributor to persistent episodes of haze throughout the Arctic [*Schnell*, 1984; *Iversen*, 1984; *Shipman et al.*, 1992; *Lamarque and Hess*, 2003], and in winter these

[1] Escuela Técnica Superior de Ingeniería de Bilbao, Universidad del País Vasco-Euskal Herriko Unibertsitatea, Bilbao, Spain.
[2] Fundación Centro de Estudios Ambientales del Mediterráneo, Parque Tecnológico, Paterna, Valencia, Spain.

0148-0227/06/2005JD005941

pollutants can travel around the northern edge of the Siberian High to east Asia: model studies and back-trajectory analysis have shown that about 40% of the air arriving in east Asia in winter may be polluted by European sources. This type of export pathway is at a minimum in summer [*Newell and Evans*, 2000].

[5] During the warm season, there is a persistent southward flow of European pollution into the Mediterranean at the lower troposphere, channeled along the gaps of the main mountain chains at the northern coasts of the Mediterranean. Stably stratified once it enters the sea, this polluted air mass is forced to cross the Mediterranean from west-to-east, driven by the pressure gradient between the Azores anticyclone and the low-pressure system at southwestern Asia [*Millán et al.*, 1997]. The Etesian winds at the eastern Mediterranean [*Kallos et al.*, 1993], generated by venting of the Black Sea along the Bosporus and Dardanelles straits, and the Tramontana and Mistral jet-like flows at the Gulf of Lyon in the western Mediterranean basin (WMB) [*Gangoiti et al.*, 2001], are part of the wind pattern responsible for the import of pollutants from southern Europe into the Mediterranean. Experimental evidence of the consequences of this transport of pollutants along the Mediterranean were reported by *Luria et al.* [1996], who described sulfate aerosol episodes over the coast of Israel during the warm season, which could not be attributed to local emissions. After this evidence, *Kallos* [1997] and *Kallos et al.* [1998] showed that emissions from southern Italy, Greece, and the western Anatolian Peninsula can reach the Middle East and penetrate even deeper into the African continent, crossing the coasts of Libya and Egypt, into the eastern Sahel and the Intertropical Front (ITF) region, within a time period of 4 to 6 days.

[6] These advective processes in the eastern Mediterranean contrast with the typical daily circulatory cycles in the WMB. European pollution entering the Mediterranean with the Mistral and Tramontana winds through the Gulf of Lyon, together with fresh local emissions, are trapped in the coastal recirculations [*Millán et al.*, 1992, 1996, 1997] and the atmospheric gyre [*Gangoiti et al.*, 2001] of the western basin. This type of mesoscale circulation generates stably stratified reservoir layers between the sea surface and the 4 km altitude, where European pollutants accumulate, and helps to maintain high O_3 background concentrations (50–65 ppb) at the coastal and inland monitoring stations of eastern Iberia during the whole warm season [*Millán et al.*, 1996, 1997, 2000]. A significant fraction of pollutants can remain within the area for a period of up to 5 to 10 days [*Gangoiti et al.*, 2001], before being swept away after the passage of a midlatitude low-pressure system (perturbed period). Similar processes have also been documented in the central Mediterranean [*Fortezza et al.*, 1993; *Georgiadis et al.*, 1994; *Orciari et al.*, 1998].

[7] Experimental evidences of these ozone reservoir layers and circulations in the lower troposphere of the Iberian Peninsula and the western and central Mediterranean basin were gathered by successive European Projects beginning at the end of the 1980s: the pioneering Project MECAPIP (MEteorological Cycles of Air Pollution in the Iberian Peninsula), 1988–1991, and the projects RECAPMA (Regional Cycles of Air Pollution in the West Central Mediterranean Area), 1990–1992, SECAP (South European Cycles of Air Pollution), 1992–1995 and TRAPEM (Transport and Transformation of Air Pollutants on the East Mediterranean), 1992–1995.

[8] Not only does the local and regional accumulation of European pollutants over the Mediterranean have a direct impact on the air quality of the area, it can also affect the hydrological cycle of the basin, both locally and at very distant continental areas [*Millán et al.*, 2005]. Observed rainfall reductions in the eastern Sahel, in the 1970s and 1980s, have been associated with a cooler Mediterranean SST [*Lelieveld et al.*, 2002], concurrent with the main sulfate aerosol forcing of the European emissions. Subsequent reductions in sulphur-dioxide emissions during the 1990s and a warmer Mediterranean during the last 2 decades (*Rayner et al.* [1996], updated) are coincident with both the observed recovery of rainfall in the eastern Sahel [*Nicholson et al.*, 2000], and the increase in torrential rains in the western Mediterranean and adjacent regions [*Millán et al.*, 2005]. Mineral dust mobilization in northern Africa is also enhanced after a rainfall reduction in the Soudano Sahel region [*Prospero and Lamb*, 2003] and, as a consequence, a reduced heating of the TA due to an increase in dust transport by the trade winds contributes to interhemispheric TA SST anomalies that have been associated with the Soudano Sahel drought [*Lamb and Peppler*, 1992; *Ward*, 1998]. Thus the export of European pollutants across the Mediterranean and northern Africa can be playing an important role in the redistribution of rainfall in the whole region and the effects of these pollutants may extend to the TA, closing another feedback cycle at the intercontinental scale. How this possible role fits with other important climatic forcings driving the rain distribution over the area, such as the changes in the SST of the equatorial oceans [*Giannini et al.*, 2003] and the ocean circulation, changes and interactions with the land use and vegetation cover [*Zeng et al.*, 1999] and the possible role of the variations in the primary productivity of the oceans[*Falkowski et al.*, 1998; *Michaels et al.*, 1996; *Jickells et al.*, 2005] modulated by the dust transport to the oceans, are important questions to be answered.

[9] Although the import of European pollution into the Mediterranean is well documented, the venting of the basin, mainly through northern Africa and the Middle East, is poorly understood. There are evidences of feeding into the trade winds further south: soil dust could be lifted and mixed into the polluted air mass, after crossing the southern coast of the Mediterranean, during its transit over the Sahara and Sahel regions. The joint plume of soil dust and European pollution would then traverse the coast of west Africa into the trade wind regime to cross the northern TA into the Caribbean in a transit time of 1 to 2 weeks, as proposed by *Hamelin et al.* [1989] after the identification of European lead isotopes in aerosol samples collected at Barbados from 1969 to 1987.

[10] High aerosol nitrate concentrations at Barbados have also been associated with transport from Europe and North Africa [*Savoie et al.*, 1992]. More recently, after the Atmosphere Ocean Chemistry Experiment (AEROCE), the anthropogenic contribution to the total non-sea-salt sulfate (nss SO_4^{-2}) found yearly in Barbados from July to October, was estimated to range between 60% and 80% [*Savoie et al.*, 2002]. This contribution decreases to 0–40% from November through January, following the variations in the

transport pathways of pollutants from Europe and the Mediterranean coastal region of North Africa and of dust from the Sahara and Sahel to the Caribbean [*Savoie et al.*, 2002]. However, all the summer transport pathways from the main European sources to the Caribbean, their relative contributions to the pollution burden, and the controlling dynamics and timescales of such transport need to be investigated.

[11] The work presented here makes use of a mesoscale high-resolution atmospheric model coupled with a dispersion model to establish source-receptor relationships and link the European-North African aerosol episodes observed at the Caribbean, and occurring every year during the summer period, with their main sources in Europe. State-of-the-art mesoscale atmospheric models can now simulate the meteorology of large regions with the desired degree of detail, after a selection of the required resolution, and help to describe and understand complex transport patterns over vast regions.

[12] The paper is organized as follows: mean flow regimes for the lower and middle troposphere, their interannual variations, and the prevailing meteorology during the selected period of simulation are presented and analyzed in section 2. The modeling system, and selected initial and boundary conditions are described in section 3. Section 4 is devoted to the discussion of modeling results and their comparison with concurrent instrumented aircraft observations (RECAPMA campaign) and TOMS data from the Nimbus 7 satellite. The main conclusions are summarized in section 5.

2. Mean and Perturbed Circulations During the Period of Simulation

[13] We analyze here the prevailing meteorology during the period of simulation and evaluate how representative the studied situation is when compared to a 5-year average. This analysis also helps to show the spatial coverage of the circulations governing the outflow of Mediterranean pollution, in order to select an adequate extension for the simulation domain. Figure 1 depicts mean prevailing winds and geopotential heights at 1000 hPa and at 700 hPa during the period selected for simulation (15 July to 16 August 1991). The raw data used come from the National Centers for Environmental Prediction, provided by the NOAA-CIRES Climate Diagnostics Center's (Boulder, Colorado, USA) Web site at http://www.cdc.noaa.gov/, with a horizontal resolution of $2.5° \times 2.5°$ ($4 \times$ daily global reanalysis data). Selected fields have been processed to represent averages at 0600 UTC and 1800 UTC, to separate diurnal variations of the planetary boundary layer (PBL) flows driven by the solar cycle. Schematic air mass trajectories are also shown, representing the inferred "average transport" pathways for southern Europe and northern Africa emissions.

[14] Dry convection over the northern Africa landmass (colored in blue in Figure 1e), vertically mix and couple the Mediterranean marine boundary layer (MBL) flow with the northeasterly winds over eastern Tunisia, Libya and Egypt blowing at 700 hPa and then flowing over the Sahara and Sahel region (Harmattan trades). This dry and hazy wind intensifies during daytime as a response to the deepening of the low-pressure systems over central Africa and SW Asia (Figure 1: notice the wind intensification in the right plots), and it can transport dust and European pollution from the Mediterranean into the TA within the SAL (see sections 4.2 and 4.3).

[15] Figure 1e shows the mean total atmospheric precipitable water during the period of simulation. Convergence at lower levels (Figures 1a and 1b) in regions of high values of total precipitable water (in red in Figure 1e) makes those regions more likely subject to deep convection and precipitation scavenging. Conversely, air subsidence within the SAL above the Sahara and Sahel region, with the lowest values of total precipitable water, inhibits moist convection and wet removal of mineral dust and pollutants. These mechanisms working at different latitudes over the African continent will contribute to the observed latitudinal (northward) migration of the Saharan dust plume during the warm season [*Prospero et al.*, 2002], following the onset of the southwest monsoon, and make the southernmost pathways, shown in Figure 1, less effective for transporting pollution to the western Atlantic. Transport at the lowest levels (below 1000 m MSL) from the western coast of Africa to the Caribbean, shown in Figures 1a and 1b, can incorporate pollution, traveling directly from western Iberia and/or vented from the Mediterranean through Gibraltar, as well as trapped African continental pollution (transported by the Harmattan's, which blow above the coastal MBL) from vertical mixing within the sea breeze convection cells at the west coast of Africa.

[16] Another important feature in Figures 1c and 1d is the high-pressure system over northern Africa at 700 hPa, which could recirculate back to the Mediterranean an important fraction of pollutants imported through the coast of eastern Tunisia and Libya. Over the western coast of Africa, above latitude 20°N, winds (parallel to the coast) reverse from northerly, at the MBL and up to the trade-wind inversion, to southerly at 700 hPa. This will probably cause trapping of the European pollution and soil dust contained in the SAL within the coastal land and sea breeze cells of the western coast of Africa, with higher residence times for the trapped air masses (section 4.3).

[17] To evaluate the interannual variability of the regional meteorology and test whether the selected period of simulation represents "mean summer" meteorology over the area, multiyear averages of wind and pressure fields have been estimated. Figures 2a–2d show these averages for a 5-year period (1998–2002), from 15 July to 16 August. The main differences between both figures are centered at latitudes above 45–50°N. In 1991, the low-pressure systems between Greenland and Iceland were deeper than the average, affecting the circulation over the northern Atlantic. However, these differences are within the range of the expected variations at these latitudes. Figures 2e and 2f show the standard deviations of the 1000 hPa geopotential height field. Values larger than 65 m in the geopotential height have been calculated for this area for the 5-year record. In contrast, low interannual variations (less than 25 m, and decreasing with latitude) are observed for the Mediterranean, northern Africa and the TA. The same is true for the whole warm season, but this does not hold for winter conditions. *Duncan and Bey* [2004] also show that export

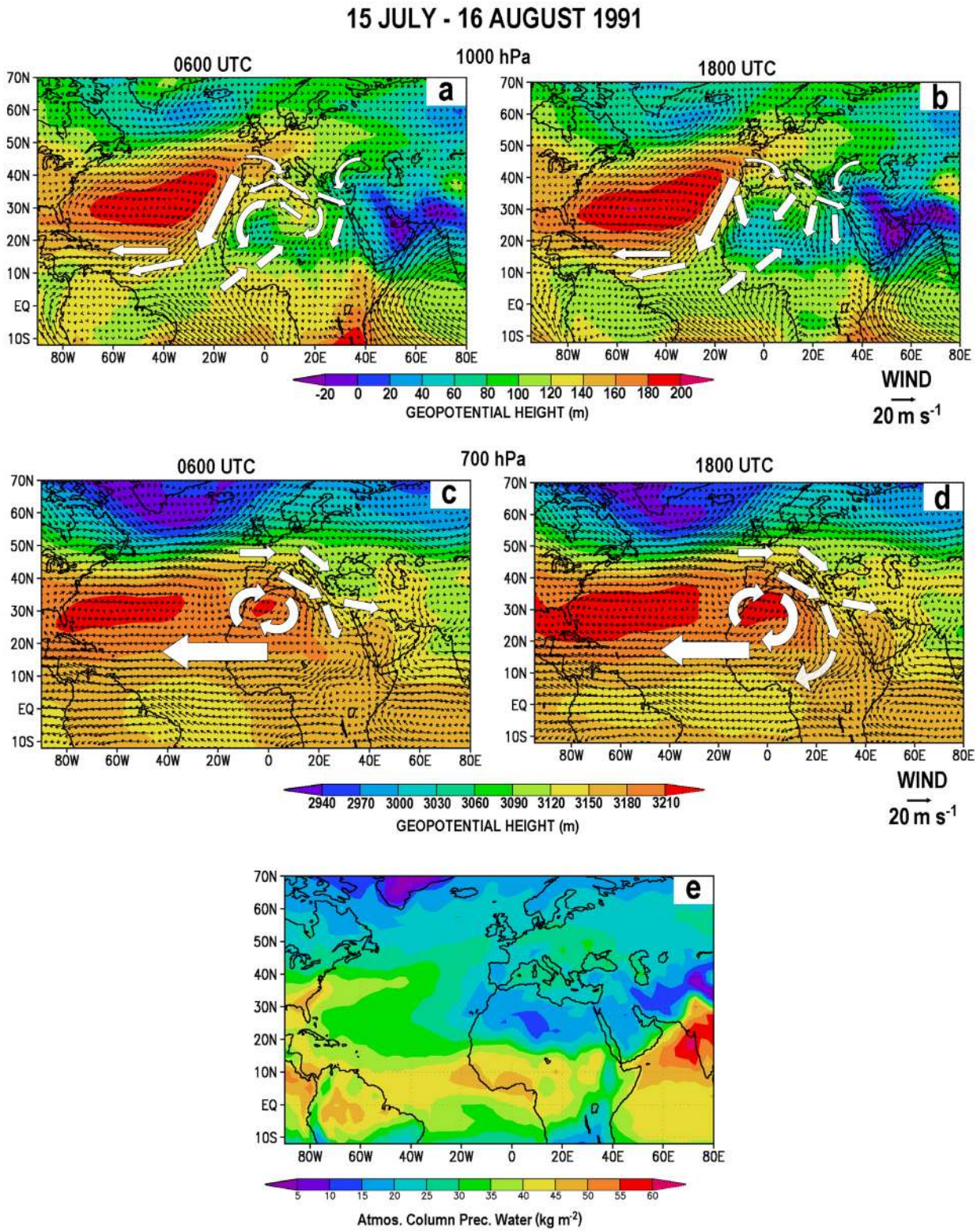

Figure 1. Mean prevailing winds and heights of the 1000 hPa surface for the analysis period (from 15 July to 16 August 1991) at (a) 0600 UTC and (b) 1800 UTC. Same for the 700 hPa surface at (c) 0600 UTC and (d) 1800 UTC. (e) Total atmospheric column of precipitable water averaged over the whole period. Main pathways (white arrows) for the export of pollutants from southern Europe and the Mediterranean into the TA are more likely at upper levels (Figures 1c and 1d). A direct pathway from western Iberia is observed at lower levels (Figures 1a and 1b). Convergence of European pollution over the Sahara and Sahel regions and dry convection (Figure 1e) over the area draw pollutants to the main exportation pathway at upper levels.

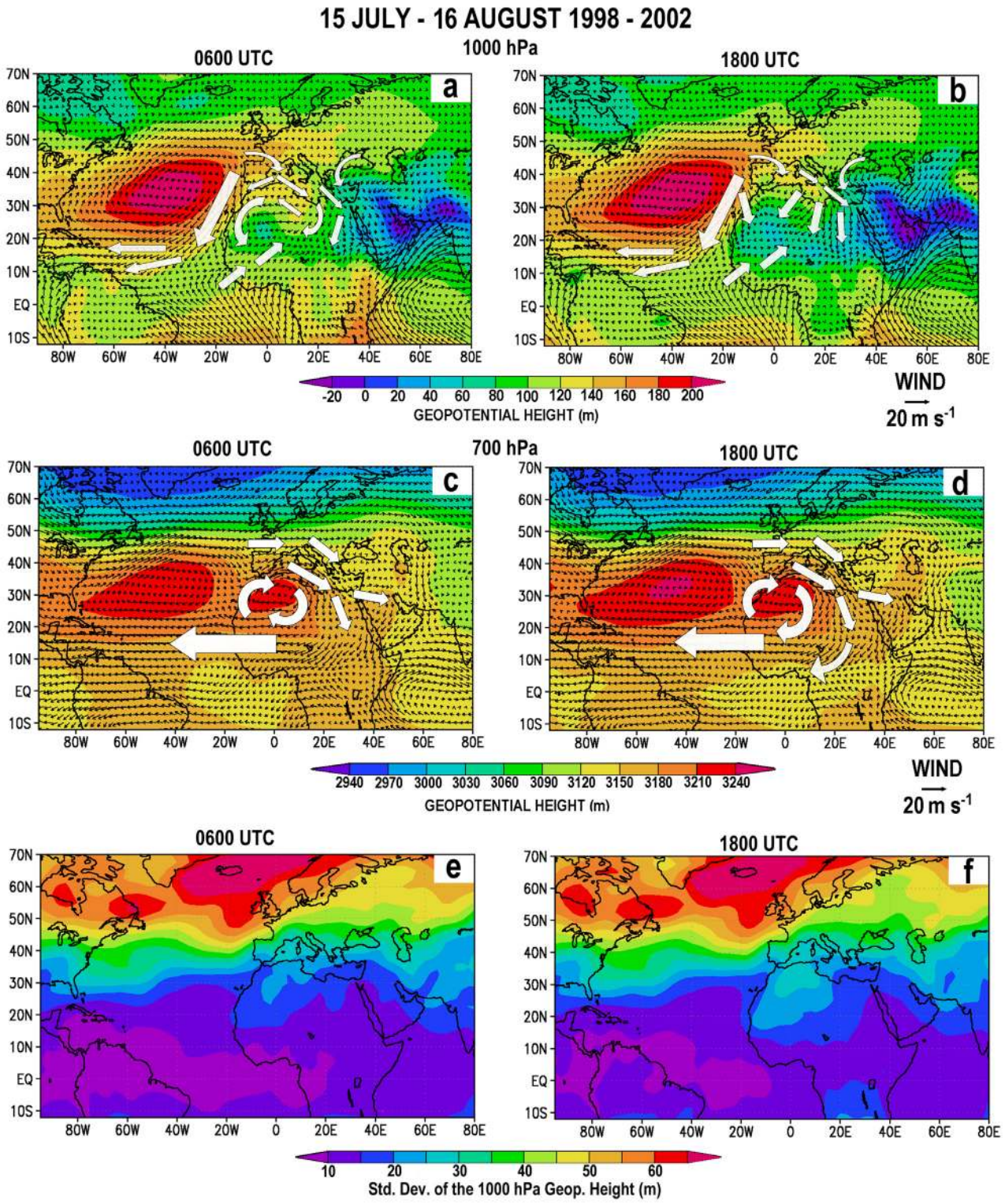

Figure 2. (a–d) Same as Figures 1a–1d but for a 5-year period (1998–2002). The standard deviation of the 1000 hPa geopotential heights at (e) 0600 UTC and (f) 1800 UTC is also represented.

pathways of European pollution in summer vary less from year to year than in winter.

[18] The prevailing meteorology during the RECAPMA flight campaign (16–19 July 1991) and the following days up to 16 August is summarized in Figure 1; it shows that the mean meteorology over the region represents normal conditions (section 4.1). Nevertheless, after observing important changes in the tracer transport pathways between 28

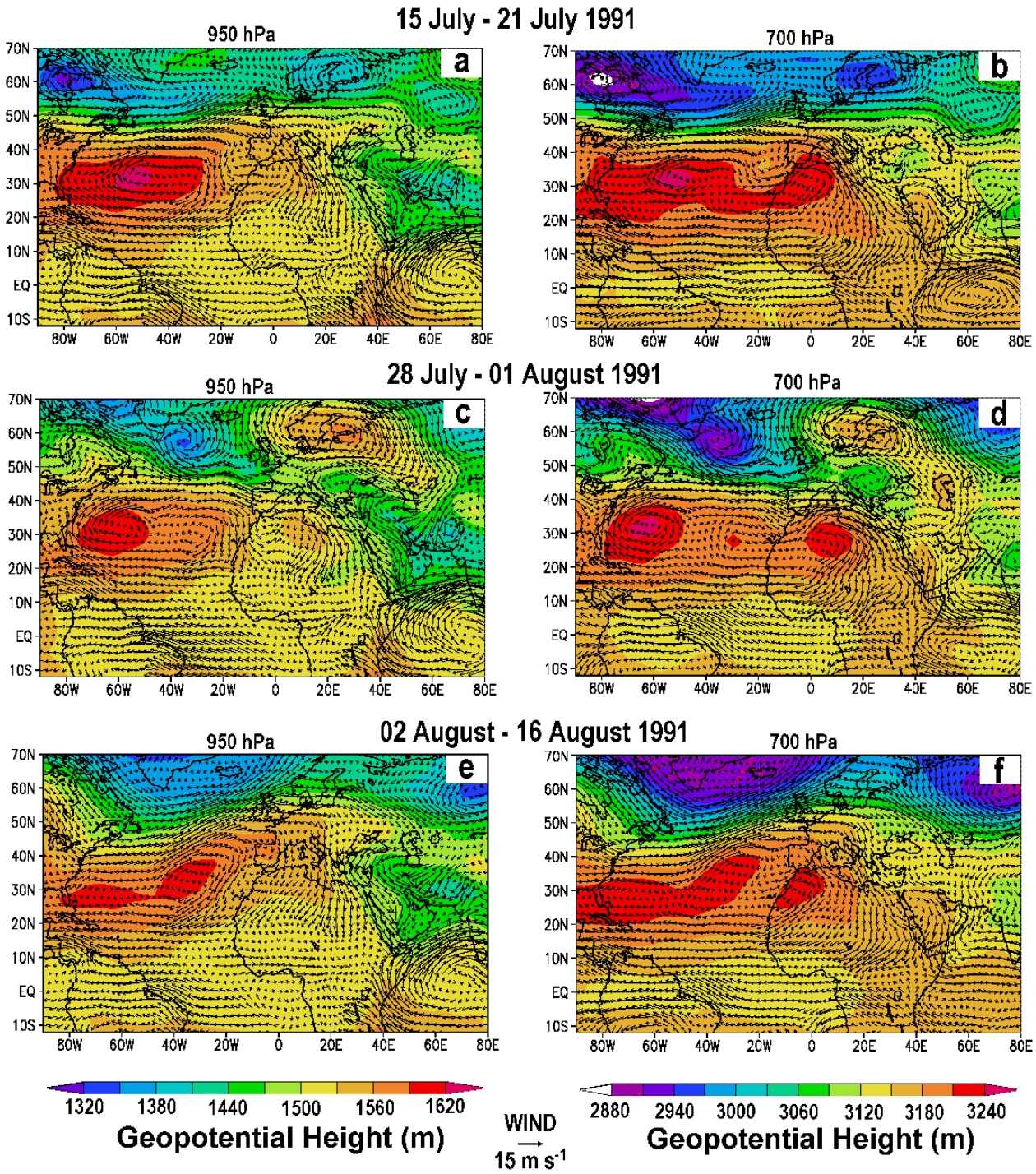

Figure 3. Three main meteorological periods observed from 15 July to 16 August 1991, obtained after processing the 4× daily global NCEP/DOE Reanalysis-2 data set: (a) Mean prevailing winds and heights of the 950 hPa surface during normal (close-to-mean) synoptic meteorology over northern Africa for the period 15–21 July 1991. (b) Normal conditions during the same period for the 700 hPa surface. Same meteorological fields (c and d) for the perturbed conditions from 28 July to 1 August and (e and f) for the restored normal conditions during the last period of the simulation from 2 to 16 August.

and 31 July over northern Africa (section 4.2), we concluded that in spite of the small variability inferred from the prevailing wind regimes and general meteorological conditions (Figures 2e and 2f), disturbances can burst into the area for short periods and alter pollutant/dust transport in the whole region. Normal and perturbed meteorological conditions are now summarized in Figure 3. The simulation period is subdivided into three

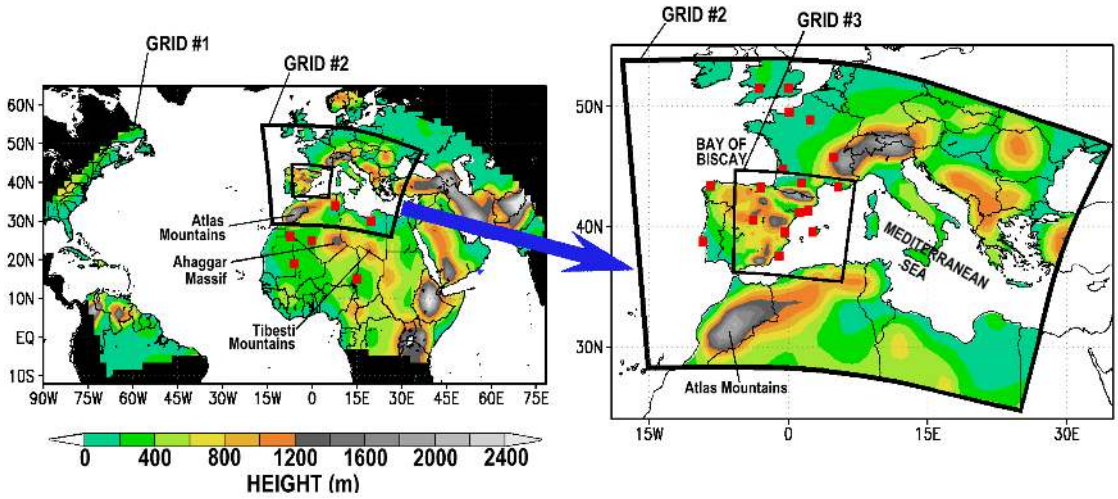

Figure 4. (left) Topographic map of the three domains (grids 1, 2 and 3) used by RAMS with the African dust sources (solid red squares) selected for the simulations. (right) Enlarged view of the medium-size (grid 2) and smallest (grid 3) domains. The selected European sources of pollution are represented with solid red squares.

main parts: normal (close to average) conditions during the first week (15–21 July: Figures 3a and 3b), followed by a perturbed situation, which is well developed during the period 28 July to 1 August (Figures 3c and 3d), and the return to normal conditions from 2 to 16 August (Figures 3e and 3f).

[19] During normal conditions, the Azores Anticyclone extends a ridge of high pressure over the Bay of Biscay and France, and the west-to-east passage of midlatitude low-pressure systems is confined to higher latitudes. During this period, WMB diurnal cycles are well developed and our simulations reproduce daily pulsations similar to those observed by *Gangoiti et al.* [2001] during the flight campaign of the RECAPMA project (section 4.1), but with a different grid arrangement (section 3).

[20] The perturbed conditions (Figures 3c and 3d) are built up after a period of several days in which the Azores high extends to higher latitudes and breaks up into two cells. The northernmost cell locates over the Scandinavian Peninsula on 28 July and blocks the eastward passage of midlatitude low-pressure systems, while the southern Azores high cell is drawn out of the Bay of Biscay back to the Atlantic Ocean. Frontal systems and troughs can now extend further south, following a NW-to-SE direction, and perturbations are observed crossing the Bay of Biscay and France, between the Azores and the Scandinavian highs. This results in a strong western advection of maritime Atlantic air at the WMB and the northwestern coast of Africa, which vents the area and pushes the anticyclonic 700 hPa circulation eastward over northern Africa. The consequence is a complete redistribution of dust and pollutants in the region (to be discussed in the following subsections). Two other smaller perturbations crossed the WMB during the period of simulation: their effects were not detected in northern Africa, although they affected the WMB circulations (section 4.1).

3. Modeling System: Initial and Boundary Conditions of Simulation

[21] After we succeeded in describing both the import of European pollution into the Mediterranean during the flight campaign of the RECAPMA project in July 1991 [*Gangoiti et al.*, 2001] and the observed daily recirculatory bimodal pulsation of the wind field in the WMB, we were encouraged to use a similar model system to evaluate the export pathways of European emissions from the Mediterranean. The Regional Atmospheric Modeling System (RAMS version 4.4.0 [*Pielke et al.*, 1992]) is used now with a larger domain (Figure 4) and time period (32 days) to simulate the atmospheric processes at a sufficient temporal and spatial resolution. Latest versions of the code, as the one used here, allow parallelization, which helps to shorten computer time. Wind and turbulence fields obtained by RAMS are fed to the HYbrid PArticle Concentration and Transport (HYPACT) model, which is a combination of a Lagrangian particle model and an Eulerian concentration transport model [*Tremback et al.*, 1993]. Almost any type of source can be specified anywhere in the simulation domain with instantaneous, intermittent or continuous emissions.

[22] RAMS is a nonhydrostatic prognostic model with a highly versatile numerical code. For both the RECAPMA project and the present simulations, we selected a nonhomogeneous initialization with nonstationary boundary conditions. The 32 days simulated include the flight campaign during the first week and subsequent days up to 16 August. This extended period allows tracking of pollutants at an intercontinental scale. Three nested grids are used for the simulation: the finest grid (grid 3 in Figure 4), which is run

with a 24-km cell size, and the medium grid (grid 2 in Figure 4) with a 96-km grid cell, are kept at a location and coverage similar to those of the RECAPMA simulations [*Gangoiti et al.*, 2001]. Thus the consistency of new simulations over the Mediterranean with flight observations can be checked, as well as the observed diurnal pulsation of the MBL and free troposphere over the area. The largest and coarsest grid (grid 1 in Figure 4), with a 192 km grid cell size, extends the coverage to the TA, America and most of Africa, Europe and western Asia.

[23] For all the domains 34 vertical levels with variable resolutions are used, with a total coverage of 12,000 m. Resolutions of 25–40 m near the ground and of 1000 m at the highest levels are selected. Two-way nesting is allowed between the grids, so that the higher-resolution grid conditions the flow in the lower-resolution grid and vice versa. Four-dimensional data assimilation is used for the model run, nudging the boundaries of the larger grid to the conditions given by the NCEP reanalysis daily data at 0000, 0600, 1200 and 1800 UTC. The run was performed continuously, from 0000 UTC on 15 July 1991 through 0000 UTC on 16 August 1991. The topography and land cover were interpolated to the model grids from the USGS global 30″ lat-long database (http://edcdaac.usgs.gov/glcc/glcc.asp). Raw SST data (weekly averages) with a resolution of $1^\circ \times 1^\circ$ were interpolated to the model grids from the NCEP Reynolds SST data set [*Reynolds and Smith*, 1994], (available at ftp://podaac.jpl.nasa.gov/pub/sea_surface_temperature/reynolds/oisst). As the model run extends for more than 4 weeks, SST values are automatically interpolated in time during the model run. Our model setup includes a prognostic turbulent kinetic energy (level 2.5) parameterization [*Mellor and Yamada*, 1982], with modifications for a case of growing turbulence [*Helfand and Labraga*, 1988], a full-column two-stream single-band radiation scheme that accounts for clouds, and calculations of shortwave and longwave radiation [*Chen and Cotton*, 1983]. The cloud and precipitation scheme by *Walko et al.* [1995] was applied in all the domains. The soil vegetation scheme LEAF-2 is used to calculate sensible and latent heat fluxes exchanges with the atmosphere, using prognostic equations for soil moisture and temperature [*Walko et al.*, 2000].

[24] Hourly meteorological fields given by RAMS are forwarded to the HYPACT model to evaluate the dispersion of an atmospheric passive tracer. Thus emitted particles do not undergo chemical transformation or any type of removal processes. Figure 4 shows the position of the selected European pollution sources, comprising a total of 17 vertical emission lines, placed at urban and industrial conglomerates in western and southern European countries. The variable height of the particle release, from surface level to 300 m above surface level, accounts for the great variety of effective emission heights in the urban and industrial environments. The coastal (Mediterranean and Atlantic) and inland sources shown in Figure 4 cover an area of different weather and wind regimes in western and southern Europe during the warm season; they were chosen to account for all the possible transport mechanisms working in the area. (1) Region A includes four cities in northwestern Europe-Atlantic: London, Cardiff, Le Havre and Paris; (2) region B includes five cities in southwestern Europe-Atlantic: Bordeaux, Bilbao, A Coruña, Lisbon and Madrid; (3) region C includes four cities in northwestern Europe-Mediterranean: Lyon, Toulouse, Marseille and Barcelona; and (4) region D includes four cities in central and southwestern Europe-Mediterranean: Tarragona, Valencia, Palma de Mallorca and Cartagena.

[25] Particle release starts 6 hours after the mesoscale meteorological model initial time of simulation and lasts for 10 days (0600 UTC on 15 July to 0600 UTC on 25 July 1991), while particle positions are tracked for the whole period of simulation (32 days). Thus mesoscale meteorology is already well developed in all the model grids at the start of the particle release, and a vast area is covered by the passive tracer after the emission of a maximum of 480,000 particles during the 10 days of continuous release from region B (384,000 particles for each of the remaining simulations: regions A, C and D). Our first trial simulations showed that if we selected a larger release period, most of the particles released after the first 10 days were still on their way out of northern Africa circulations, and occupied the central area of the larger domain at the end of the simulation period (16 August). Thus we selected a period of 10 days for the release in order to have most of the particles from European sources crossing the outer boundaries of the larger domain while keeping a lesser computational expense. Selected conditions of simulation are not intended to draw conclusions on actual pollutant burdens emitted from different European sources; they allow us to investigate in detail preferred pathways, time(s) of travel, areas of accumulation (largest time of residence) and venting mechanisms for the export of pollutants from Europe.

[26] Ground emissions (point sources) from a selection of the main mineral dust sources in the Saharan and Sahel regions have also been tracked for the same period, in a series of simulations including a set of six sources (Figure 4), which are active at least during the summer season [*Prospero et al.*, 2002; *Washington et al.*, 2003]. (1) Region 1 includes Tunisia (south of the northern Atlas Mountains); (2) region 2 includes the eastern Libyan desert; (3) region 3 includes Lake Chad basin; and (4) region 4 includes Mali, Mauritania and the western flanks of the Ahaggar mountains (3 point sources).

[27] Using point sources instead of more realistic area sources does make a difference at the local scale, but at the regional-to-intercontinental scale, we found that transport pathways and trajectories were similar for point and area sources of a limited size (1–2 cells), and could be obtained at lesser computational expense. Emitted particles are treated as passive tracers and their release is continuous and constant and does not depend on surface wind velocity. Thus we expect to have more tracer than real dust in the air for some periods (calm conditions) and less for windy conditions at the African dust sources. After the emission, the tracer will be uplifted by the turbulence and convection generated by the mesoscale model. Thus we are tracking all possible trajectories driven by the atmosphere from the dust sources, and if dust fronts are developed over northern Africa during the simulation, they should be identified by the tracer distribution and movement.

[28] For this set of simulations, a larger release period was selected (25 days), starting at 0600 UTC on 15 July. This was found necessary to have enough particles to

reproduce the TOMS aerosol index distribution during the observed transition between normal and perturbed circulations over northern Africa and the Mediterranean. This transition occurred at the middle of the simulated period (28 July to 1 August) and caused a redistribution of dust over a vast region (section 4.2). A shorter period of 10 days, similar to the European pollution simulation, would not have shown us the dust front evolution of the tracer during the perturbation because an important fraction of the tracer should have been vented out from northern Africa before.

4. Results and Discussion

[29] Three different type of results are discussed here, on the basis of observations and modeling. The first one, in section 4.1, at the regional scale (ozone circulations in the WMB). The second, in section 4.2, at the regional-to-continental scale (dust in northern and western Africa and the Mediterranean). Both ozone and dust circulations offer the opportunity of validating the dynamic processes over different subregions of the larger domain. Finally, in the third discussion (section 4.3), the European tracer study will show how these subdomains are coupled and work together in the long-range transport.

4.1. Ozone Circulations in the Western Mediterranean Basin

[30] Figure 5 summarizes the meteorological conditions on the WMB during the RECAPMA flight campaign (Figures 5a and 5b) and following days (Figures 5c–5f) after the RAMS simulations. Figures 5a and 5b show results in the grid 3: the horizontal wind at 200 m above the terrain (σ coordinate system) and the vertical wind over the sea, at 0600 and 1800 UTC, 18 July 1991. Vertical wind is depicted in shaded color on a horizontal section of grid 3, at an altitude of 200 m MSL. Grey colored areas correspond to no-data grid cells, because of terrain interception. In contrast with the early morning conditions (Figure 5a), the afternoon data (Figure 5b) show a generalized sinking of 1–2 cm s^{-1} on the sea, with smaller areas of greater downward velocities near the coast of North Africa, SW of the Balearic Islands and the Gulf of Lyon. During the evening the model also represents an easterly deflection of the jet-like flow at the Gulf of Lyon (4–15 m s^{-1}), observed in a north-to-south direction during the morning. The Mistral and Tramontana diurnal eastward deflection follows the onset of sea breezes at eastern Iberia and northern Africa, and the associated compensatory sinking motion over the WMB. The resulting clockwise rotation of the whole air shed in the basin, around a relative high-pressure vortex over the sea, will contribute to recirculate pollutants entering the basin both from coastal emissions at the western Mediterranean and more distant contributions in western Europe [*Gangoiti et al.*, 2001].

[31] The "quasi-simultaneous" winds and O_3 concentrations observed during the flight tracks of 18 July are shown in Figure 6. Flight tracks have been divided into three subtracks to show the time evolution of the records: the northern subtrack goes from Marseille to the northeast of Barcelona; the intermediate subtrack goes from this latter point, parallel to the coast, to the south of Tarragona; the southern subtrack goes from Tarragona to the north of Valencia. Figure 6 (top left) depicts the night and early morning position of the Tramontana-Mistral jet flow (10–15 m s^{-1}) over the Gulf of Lyon, and the transition to the sea breeze regime at the eastern coast of Iberia. Early morning developing sea breezes are observed at southern locations of the flights tracks in the same figure. The jet is crossing the Carcasonne gap into the Mediterranean and bringing 50–65 ppb of O_3 of continental origin (measured at the flight tracks depicted in Figure 6 (bottom left)). The O_3 concentrations over the Spanish coastal area are even higher: a large peak of 105 ppb can be seen south of Tarragona, with a horizontal extent of 30 km along the coastline. This large polluted air mass is added to a general level of 50–70 ppb of O_3, with increasing values from north to south. Afternoon data for the same day are depicted in Figure 6 (top right): the observed sea breeze from the southeast, at the coastal sites of eastern Iberia, is well represented by the model (Figure 5b), as is the eastward deflection of the Gulf of Lyon jet. The associated clockwise rotation of the air mass within the WMB piles up the pollutants at the northern flight tracks, which now show very large O_3 concentrations (75–95 ppb in a horizontal extension of 300 km, between Barcelona and Marseille) over a general "background" of 55–65 ppb, registered between Valencia and Tarragona. At this point we have been able to simulate the same atmospheric processes at regional scale as those described by *Gangoiti et al.* [2001], but with a different grid arrangement.

[32] The daily recirculation of pollutants in the WMB observed during the flight campaign represents normal conditions in the basin for the warm season: north-to-south transport of pollutants during nighttime from southern France to the northern coasts of Africa, followed by the onset of the sea breezes and the associated anticyclonic forcing of the air shed in the basin during daytime. This daily pulsation results in an accumulation of pollutants and contributes to maintain high concentrations of O_3 from March to September [*Millán et al.*, 2000; *Gangoiti et al.*, 2001].

[33] During the perturbed conditions (Figures 3c and 3d), the bimodal daily circulations in the WMB are inhibited (Figures 5c and 5d) and pollutants are vented out of the area with trajectories that cross central Europe (section 4.3). Normal conditions are restored after 1 August (Figures 5e and 5f), and the bimodal circulation in the WMB is again activated. Other perturbations, on 23 July (over western France) and on 9 August (over the WMB), did not have such an impact on the dust distribution over northern Africa (TOMS AI data) as the one observed during the period 28 July to 1 August. However, we observed an effective venting of the WMB after the inhibition of the circulatory flows, with a similar wind field as that shown in Figures 5c and 5d. The observed perturbation recurrence time in the WMB is one episode every 4 to 10 days for the summer period.

4.2. Dust Circulations in Northern Africa and the Mediterranean Region

[34] Soil dust and other absorbing aerosols over the area can be tracked using the Total Ozone Mapping Spectrometer (TOMS) onboard the Nimbus 7 satellite. As TOMS can detect absorbing aerosols (dust and smoke) in the ultraviolet

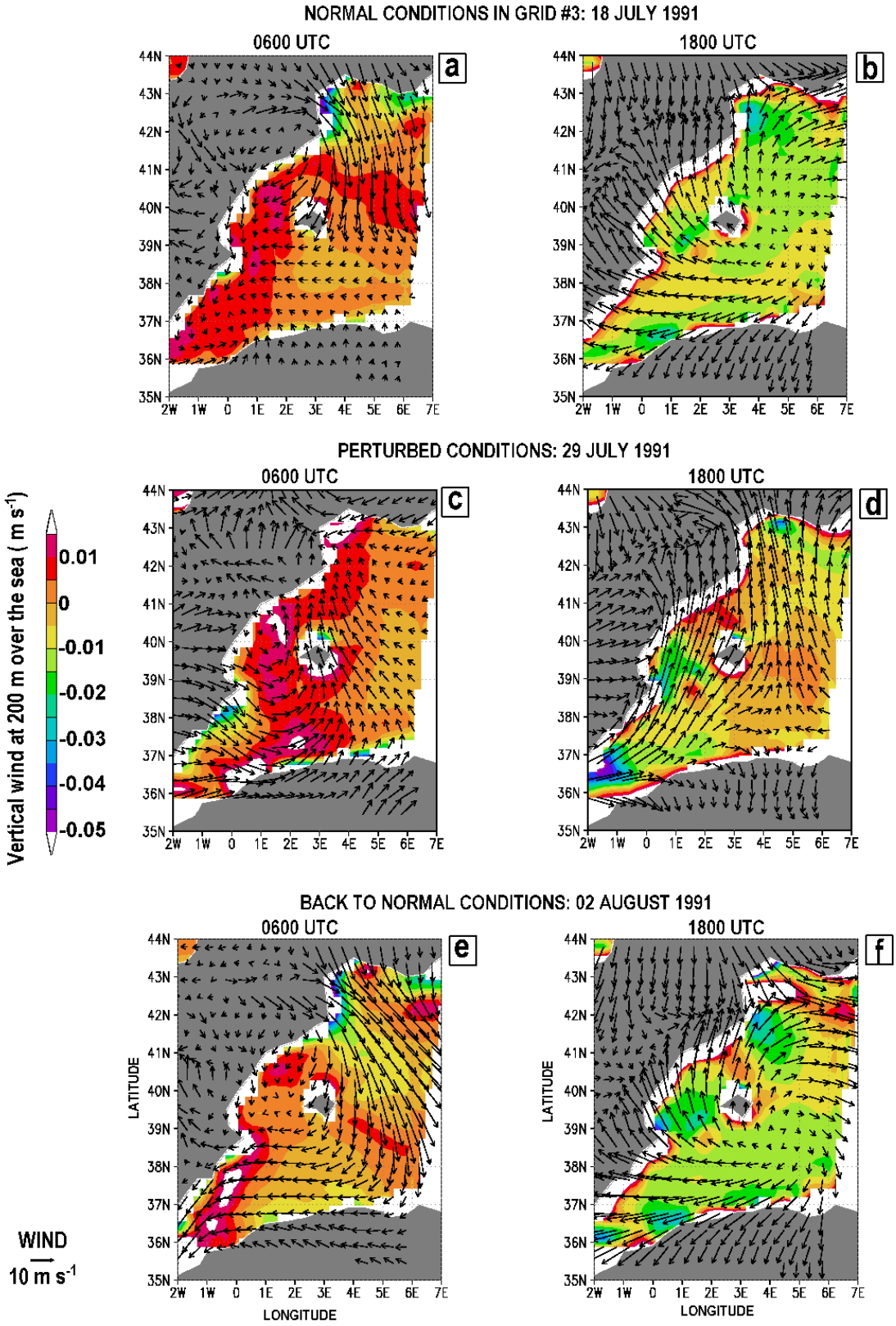

Figure 5. Sequence of characteristic wind fields on the western Mediterranean basin (RAMS model results on grid 3) during the three main periods presented in Figure 3: Horizontal wind field at 200 m above ground (σ coordinate system) and vertical wind (only over the sea, in shaded colors) at (a) 0600 UTC and (b) 1800 UTC for 18 July 1991. Same meteorological fields (c and d) for the perturbed condition at 0600 UTC and 1800 UTC on 29 July 1991 and (e and f) for the restoration of normal conditions over the western basin.

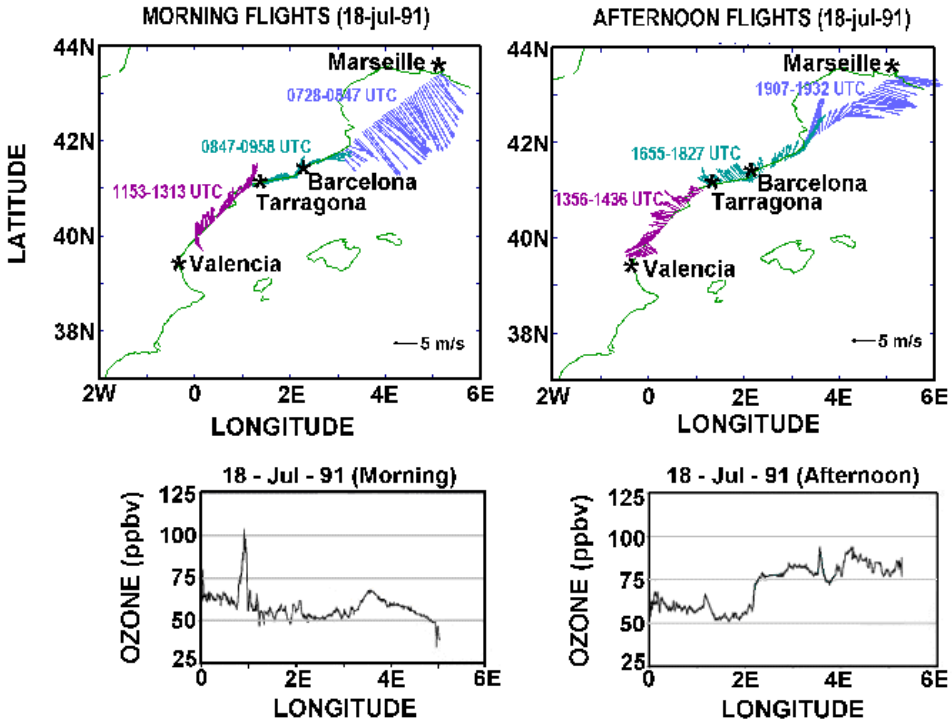

Figure 6. RECAPMA flight campaign results under normal conditions in the western Mediterranean basin (18 July 1991): horizontal winds and O_3 concentrations at marked flight tracks (150–200 m MSL) (left) during the morning-to-afternoon transition and (right) during the afternoon/evening. UTC flight time is shown for each subtrack. The wind scale is also depicted in the figure. See Figures 5a and 5b for comparison with model results.

spectrum over land and water surfaces [*Herman et al.*, 1997], it can observe the occurrence of large dust events over the African continent, and follow the continuity of these plumes over the oceans. We use the aerosol index algorithm (AI), described by *Herman et al.* [1997] and *Torres et al.* [1998], to track the Saharan dust over northern Africa and the Mediterranean during the period of simulation. Raw data with daily AI distributions at a linear latitude/longitude projection with a resolution of 1 × 1.25° [*Herman et al.*, 1997], were obtained from the NASA FTP site (ftp://jwocky.gsfc.nasa/gov/pub/nimbus7/data). Daily AI distributions in both normal and perturbed meteorological conditions have been analyzed together with modeled HYPACT dust plume distributions from the selected sources in northern Africa (section 3). The AI is not a quantitative measure of aerosol concentration. It is sensitive to a number of aerosol physical properties and to the altitude of the aerosol layers, with a lower detection capability near the surface [*Torres et al.*, 1998]. Nonetheless, most of the transport over Africa occurs above 2–3 km altitude and *Chiapello et al.* [1999] have shown that the TOMS AI provides a remarkably accurate picture of mineral dust distribution over both continental (including the Saharan desert) and oceanic regions.

[35] Figure 7 (left) shows the TOMS absorbing AI in shaded colors together with the marine layer airflow (red arrows), inferred from the RAMS simulations during normal conditions (23 July 1991) at northern Africa. Also shown in Figure 7 are the 2-day (31 July to 2 August) sequence in the evolution of the dust plume during the perturbed conditions up to the restitution of normal conditions and, finally, the fully developed normal conditions, on 6 August, with venting to the WMB around the Atlas Mountains (northern slopes) and over the Canary islands. Nimbus 7 TOMS reflectivity data are likewise depicted on the same set of figures (ftp://jwocky.gsfc.nasa/gov/pub/nimbus7/data) to map the areas covered by clouds. At these sites, the dust plume is not visible (near-zero values for the AI) and precipitation scavenging of aerosols and highly soluble gases is more likely to contribute to depletion of the mineral dust and pollution burden in the air mass. Vertical mixing and upper troposphere venting are also more effective where moist convective mechanisms are active.

[36] Figure 7 (middle) shows the same sequence for the particle concentration simulated by HYPACT (vertically integrated) together with the observed cloud cover (TOMS reflectivity). Winds simulated by RAMS at 3600 m above the terrain (σ coordinate system), shown in Figure 7 (right), help to understand the flow dynamics driving the dust plumes. Similarities between observed (Figure 7, left) and modeled (Figure 7, middle) dust distributions are shown in terms of the circulation-driven patterns observed in Figure 7:

[37] 1. The dust plume over the WMB and northern slopes of the Atlas Mountains, under normal conditions (AI in the first and last row of Figure 7), follows the circulation around the Atlas mountains at high altitude. The tracer distribution, in the middle plots, shows similar

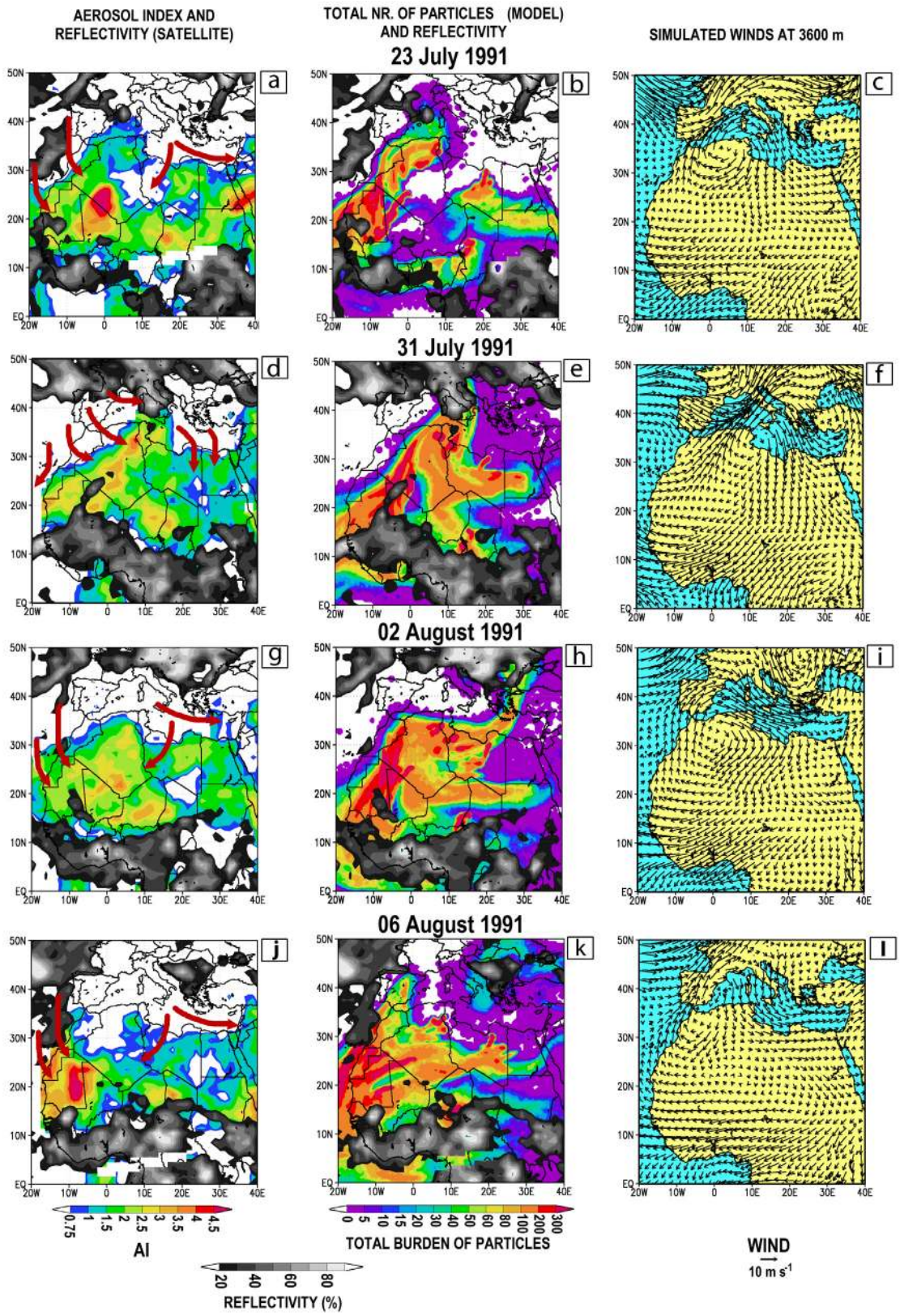
AEROSOL INDEX AND REFLECTIVITY (SATELLITE)
TOTAL NR. OF PARTICLES (MODEL) AND REFLECTIVITY
SIMULATED WINDS AT 3600 m
23 July 1991
31 July 1991
02 August 1991
06 August 1991
a
b
c
d
e
f
g
h
i
j
k
l
AI
0.75 1 1.5 2 2.5 3 3.5 4 4.5
TOTAL BURDEN OF PARTICLES
0 5 10 15 20 30 40 50 60 80 100 200 300
REFLECTIVITY (%)
20 40 60 80
WIND
10 m s-1

Figure 7

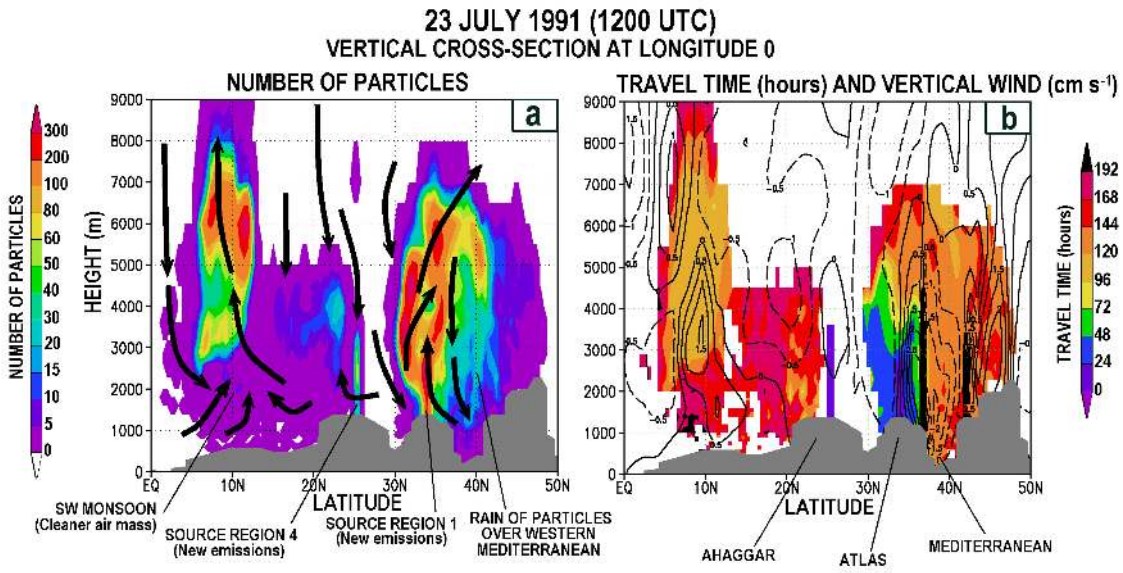

Figure 8. (a) Vertical cross section, centered at constant longitude 0, of the dust plume distribution in Figure 7b (1200 UTC, 23 July 1991). Total number of tracer particles between longitudes 0 and 10°E are depicted together with main vertical air movements (black arrows). (b) Mean age (shaded colors) of the dust plume cross section and vertical winds (in contour lines): solid line for positive-upward and dash for negative-downward. The terrain profile is included at the bottom.

patterns of convergence to that region (located outside the dust production regions).

[38] 2. Dust divergence over the coast of Libya, at the same panels (normal conditions), is also well represented by the tracer distribution.

[39] 3. The frontal dynamics of the dust plume during the perturbed period (AI in the second and third row of Figure 7) is also well represented by the tracer distribution: the dust front over northern Africa and the central Mediterranean is correctly positioned and seems to be synchronized with the observed dust plume dynamics during the massive turnaround (see below).

[40] A detailed discussion on both normal and perturbed circulations at northern Africa follows.

4.2.1. Normal Circulations at Northern Africa

[41] Figure 8 (left) presents a cross section of the simulated dust distribution in Figure 7b, at constant longitude 0° (1200 UTC, 23 July 1991). Latitudinal dust distribution (total number of particles between 0° and 10°E (shaded colors)) is depicted together with the main vertical air movements (black arrows) estimated by the mesoscale model. Figure 8b shows (in shaded colors) the travel times for the same dust distribution, estimated by HYPACT, and the modeled vertical winds (contour lines, solid for positive-upward and dashed for negative-downward). Vertical winds and particle travel times in Figure 8b were averaged between both longitudes. The terrain profile used by the mesoscale model is also included in Figure 8. Figure 8 allows us to analyze the latitudinal variations in the height of the SAL during normal conditions and, together with Figure 7, helps us to find the mechanisms behind the observed dust distribution.

[42] Two main dust plumes are observed in Figure 8. Under normal conditions the northern plume is driven by surface convergence and anticyclonic circulation above the 700 hPa pressure level at northwestern Africa. Source regions 1, 2 and 4 are the main contributors. The Atlas Mountains play an important role in the vertical and horizontal extension of the plume. The southern plume, which reaches higher altitudes, is driven by the Intertropical Convergence ENE trade winds over the African continent, together with the Atlantic southwest monsoon. Dust sources in regions 2 and 3 are the main contributors. The Atlantic monsoon and the position of the ITF are responsible for the southern dust plume's vertical uplift and latitudinal movements.

Figure 7. (left) Sequence of the Nimbus 7 TOMS absorbing AI with TOMS reflectivity and marine layer airflow (arrows) at northern Africa and the Mediterranean. (middle) Total burden of tracer particles for the Saharan dust simulation together with TOMS reflectivity and (right) wind field transporting the main fraction of the Saharan dust after the RAMS simulation (right). Four snapshots of the study period 15 July to 15 August 1991 are shown: (a–c) Normal conditions (23 July 1991) prevailing over northern Africa, (d–f) a dust outbreak observed/simulated over the central Mediterranean and central Europe after a perturbation over northwestern Africa, (g–i) transition to the restoration of normal conditions, and (j–l) fully developed normal conditions after the perturbed period.

[43] The main atmospheric transport mechanisms and resulting dust distributions for the northern dust plume can be summarized as follows:

[44] 1. Anticyclonic circulation of the SAL around the Atlas Mountains generates a latitudinal stratification of dust particles by age (observed between 30 and 45°N in Figure 8b): longer travel times at the northern slopes (background dust), and fresh dust loads at the southern slopes. Fresh dust outbreaks from source region 1 can expand in vertical to 2500–3000 m MSL in less than 24 hours from their release time.

[45] 2. Progress of the plume in a NE to SW direction along the corridor between Tunisia and the western Sahara, and continuous up-slope daytime venting at the southern slopes of the Atlas (Figure 7a), push the plume up to 6000–7000 m MSL. This is in agreement with LIDAR observations by *Karyampudi et al.* [1999]. The plume from source region 1 entrains dust from source region 4 to the west, then the joint plume continues its pathway parallel to the southern slopes of the Atlas into the ocean. Before arriving at the TA, over the coast of the western Sahara, part of the plume can first be vented to the middle troposphere, within the upslope winds at the southern flanks of the Atlas, and then forced to cross their ridges into the western Mediterranean (Figure 7a), following the anticyclonic forcing at that height. The rest of the plume can either circulate around the southwestern Atlas back into southern Iberia and the western Mediterranean, or drift out into the TA over the western Sahara (Figure 7j). This subcontinental circulatory flow gives rise to the observed latitudinal stratification by age of dust particles in Figure 8b.

[46] 3. Under this transport scenario there is an important wind shear between the warm air of the SAL, transporting most of the dust load (wind field in Figures 7c and 7l), and the cleaner MBL airflow over the northern and western coasts of Africa (red arrows), including the Canary islands.

[47] 4. Air mass sinking over the sea at the WMB (between 35–44°N, in Figure 8b), developed as a response to coastal and inland convergence (section 4.1), forces an actual "rain of particles" over the MBL, as observed in Figure 8a. This dust-laden layer, flowing in a SW to NE direction over the northern flanks of the Atlas, can turn around the lower Tell Atlas (northern Atlas) as shown in Figures 7a–7c, to be transported again in the opposite direction, toward the TA. This aged air mass, with a high background dust concentration uplifted 6 to 7 days before (northern plume in Figure 8b), can again entrain fresh dust outbreaks from the dust-active regions in the long corridor between the Ahaggar massif and the southern flanks of the Atlas (including source regions 1 and 4).

[48] 5. A fraction of the aged dust plume over the western Mediterranean can escape from this northern circulatory cell, drifting within the mean west-to-east airflow over the Mediterranean (section 2) in stably stratified layers, between 2000 and 6000 m MSL. These outbreaks of dust from the northern plume can reach the eastern Mediterranean and the Middle East, and penetrate in the African continent crossing the coast of Libya and Egypt deep into the eastern Sahel, to merge with the southern plume or to be vented to the upper troposphere and rain-scavenged in the ITF storm belt.

[49] In contrast, the southern dust plume presents no such circulatory motion around the Atlas. Both dry and moist convection are relevant mechanisms in the vertical mixing and venting:

[50] 1. The main dust plume (between latitudes 8–13°N in Figure 8a) comes from source region 3 (Lake Chad basin); it has been uplifted by moist convection in the storm active area of the ITF, as shown by the solid lines in Figure 8b, which are coincident with the large area of clouds observed by TOMS at that time (Figure 7). The cleaner air layer below the plume (shown in Figure 8a, from surface to 2500 m), corresponds to the cooler SW monsoon undercutting the ENE's dust-laden Harmattan's.

[51] 2. A large area of anticyclonic sinking can be seen in Figure 8b between 10 and 35°N, separating the northern and southern plumes. In this area, daytime dry convection mixes and uplifts the dust in the lower layers (surface to 3000 m MSL in Figure 8). Two plumes are observed in this area: the fresh dust emissions at latitude 25°N coming from southern Algeria and reaching an altitude of 3500 in less than 24 hours, and the older dust plume (15–22°N) from source region 1, uplifted to an altitude of between 3000 and 5000 m MSL, during a trip of 7 to 8 days. The area of southern Algeria and eastern Mali, between 15 and 22°N, is also swept by dust from the eastern Libyan desert (source region 2), crossing between the Ahaggar massif and the Tibesti mountains under perturbed conditions (not shown).

4.2.2. Perturbed Circulations at Northern Africa

[52] Normal conditions, shown in Figures 7a–7c and 8, are disrupted by a frontal passage through northern Africa, which generates a perturbed meteorology that completely redistributes the dust, as shown in the sequence depicted in Figure 7d–7i:

[53] 1. On 31 July, MBL winds at northwestern Africa (red arrows) and the Canary Islands are coupled with upper level winds (Figure 7f). A frontal system sweeps the western and central Mediterranean, pushing westward the upper level anticyclonic circulation over northern Africa. Diurnal cycles in the WMB are inhibited, and the northern plume across the Mediterranean follows a clear frontal dynamic. Both the western Mediterranean and northwestern Africa are free of dust, while the central Mediterranean and the coast of Libya, usually clean under normal conditions, appear covered by a dense plume.

[54] 2. On 2 August, progression of the dust plume to the eastern Mediterranean is evident (Figures 7g–7i), as is the massive turnaround of the northern plume across the coasts of Libya and Egypt, penetrating deep into the eastern Sahel to merge into the southern plume, in a pathway first north to south and then east to west into the TA. A fraction of the plume involved in this massive turnaround escapes to the Middle East, traveling over the eastern Mediterranean. At the same time, normal conditions are being recovered over the coasts of western Sahara and southern Morocco: wind shear develops again between the marine layer (red arrows in Figure 7g) and the SAL layer (Figure 7i), and dust is transported again around the Atlas Mountains, above a cooler and cleaner marine layer and above the trade wind inversion over the ocean. This is also in agreement with the LIDAR observations by *Karyampudi et al.* [1999] for that area. Progression of the SAL around the Atlas Mountains to the WMB is observed in Figure 7j. The dust plume is

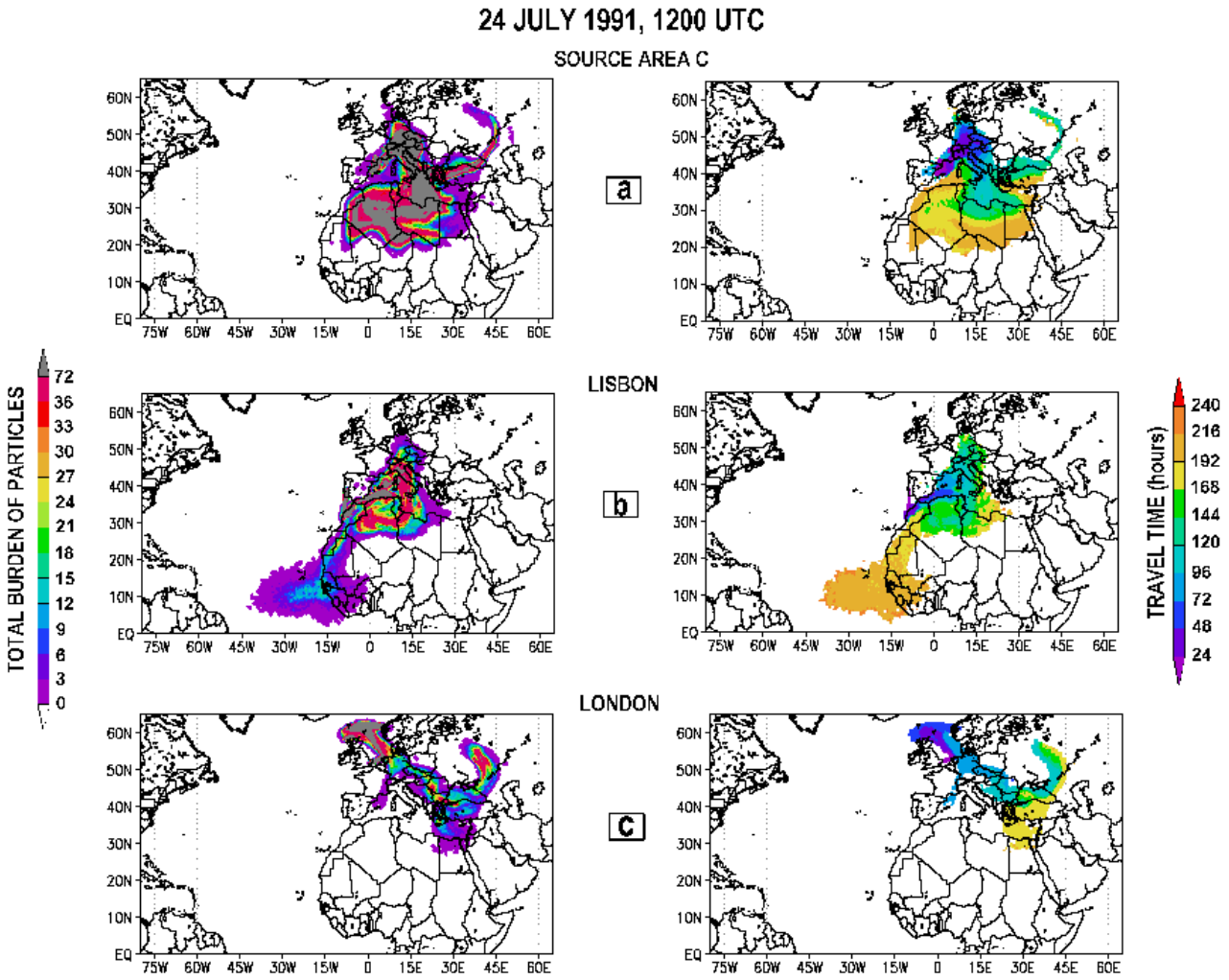

Figure 9. (left) Total burden of tracer particles for a selection of European sources and (right) mean age of the tracked pollution, 9 days after the tracer release initiation: (a) source area C (cities of Lyon, Toulouse, Marseille and Barcelona), (b) Lisbon, and (c) London.

transported now over the eastern Canary Islands and the Atlantic coast of Morocco in a slightly different pathway to the one shown in Figure 7a. Small differences between normal conditions shown in Figures 7a and 7j, arise from the slight changes in the position of the North African anticyclone (Figures 3, 7c, 7f, 7i, and 7l), responding to the evolution and proximity of the midlatitude low-pressure systems and their associated westerlies above latitude 40–45°N.

[55] With these results, the modeling system has proved capable of reproducing the main lifting and horizontal transport mechanisms related to the Saharan dust plume at northern Africa. Dust fronts are also adequately synchronized with the simulated tracer dynamics during the massive turnaround.

4.3. Intercontinental Transport of the European Tracer

[56] The European tracer, released during 10 days (15–25 July), is now tracked for the 32 days of simulation. Figures 9–16 show vertically integrated particle concentrations simulated by HYPACT, the travel time (age of the air mass) and a selection of vertical cross sections. The latter will help to show the vertical extent of convective processes and the layering under stable conditions. Figures 9–16 depict the tracer distribution at four consecutive times, which are commented in sections 4.3.1 to 4.3.4: (1) 24 July, before the perturbed conditions affected northern Africa and the Mediterranean, when most of the European tracer has already reached the African continent (section 4.3.1 and Figures 9 and 10); (2) the end of the perturbed period, 1 August, which shows the consequences in the pollution tracer distribution of the subcontinental-scale recirculations affecting the Mediterranean basin and northern Africa (section 4.3.2 and Figures 11 and 12); (3) 10 August, with normal conditions fully reestablished and after an important fraction of the European tracer reached the American continent (section 4.3.3 and Figures 13 and 14); and (4) 13 August, which shows a pollution front arrival at the Caribbean (section 4.3.4 and Figures 15 and 16).

4.3.1. Nine Days After the Initial Release Time: Initial Transport From Source Regions to the Mediterranean and the African Continent Under Normal Conditions

[57] The tracer released at Lisbon, in Figure 9b, has two preferred pathways to the TA. The first one is a direct

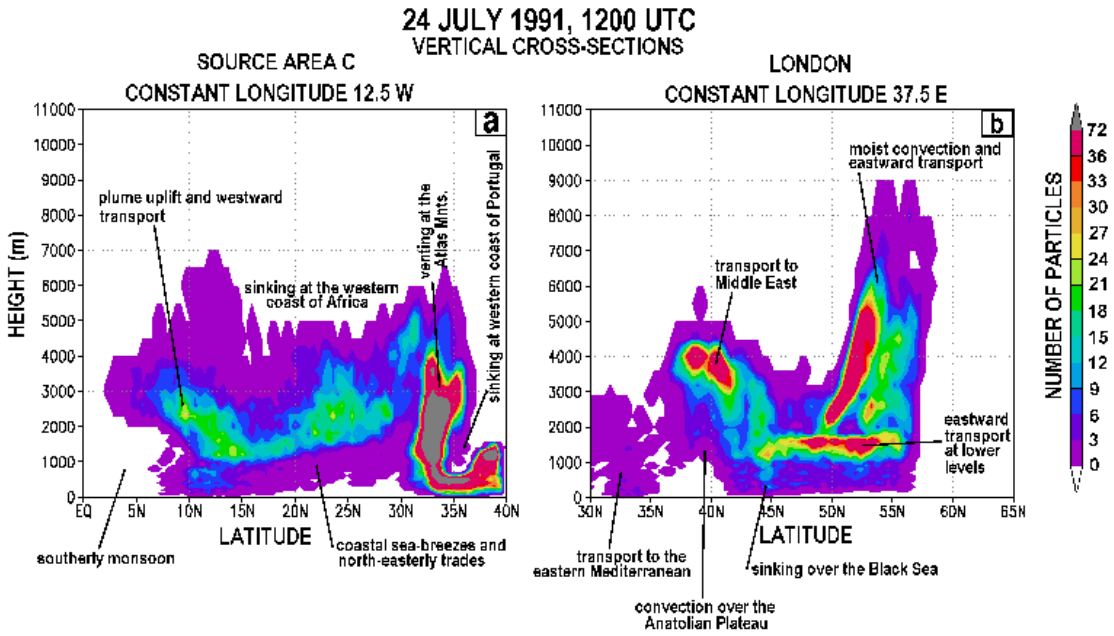

Figure 10. (a) Vertical cross section, centered at constant longitude 12.5°W (20–5°W), corresponding to the western boundary of the Lisbon tracer distribution in Figure 9b. (b) Vertical cross section, centered at longitude 37.5°E (30–45°E) (eastern boundary) of the London tracer in Figure 9c.

shortcut, parallel to the western coast of Portugal and Africa. During its southward progress from latitude 30°N to 15°N, the Lisbon tracer is uplift by the coastal sea breezes, as shown in Figure 10a (latitudinal tracer distribution centered at 12.5°W, representing the total number of particles between longitudes 20°W and 5°W). The second one is after a recirculation around the Atlas Mountains at upper levels, first entering the Mediterranean in a southwest-to-northeast direction, and then in the opposite sense after crossing the coast of Tunisia and Libya back into the TA (Figure 9b). This circulation is forced by the North African high-pressure system described in section 4.2 for normal conditions and takes place at upper levels, after vertical injection (up to 5000 m MSL) of the Lisbon tracer within the anabatic winds over the northern slopes of the Atlas (Figure 10a: latitude 32–34°N).

[58] The vertical distribution of the tracer over the western coast of Africa (Figure 10a), shows a progressive sinking of more than 1000 m for the polluted air mass in its southward drift from latitude 30°N to 15°N. Most of the pollution for this direct pathway is located above a cleaner MBL and within the trade wind inversion layer. Between 10°N and 13°N, the southerly monsoon undercuts the northeasterly trades, with two main consequences: (1) A small fraction is mixed down to the MBL and (2) most of the plume is uplifted over a cooler air layer, which pushes the trade wind inversion base up (Figure 10a). At this time the monsoon is associated with an easterly wave developing over the Gulf of Guinea (not shown), which helps first to uplift the Lisbon main plume in Figure 10a, and then to initiate its westward transport across the TA. This shortcut pathway allows the Lisbon tracer to reach the American continent in 11–12 days, and it was the preferred pathway for the first 2–3 days of the Lisbon tracer release, as shown by the travel time in Figure 9b (right). Similar pathways and dynamics were found for the tracers released at the western and northwestern coast of the Iberian Peninsula (A Coruña tracer in source region B, not shown).

[59] Most of the tracer released from region C (northwestern Mediterranean) during the first 4–5 days recirculates in the WMB following the daily cycles described in section 4.2 (not shown) and coincident with the flight campaign [*Gangoiti et al.*, 2001]. A fraction is transported around the Atlas mountains and across the coast of Tunisia, following the anticyclonic forcing aloft (Figure 9a). At the same time, another important fraction escapes from the recirculatory cell, crossing the Mediterranean basin from west to east in stable layers while traveling over water. These pollution outbreaks from the western to the eastern Mediterranean basin can be uplifted, at the coastal convective cells and islands found in their eastward drift over the sea, up to a height of 2000–4000 m [*Gangoiti et al.*, 2001]. Then, most of the fraction at the eastern basin crosses the coast of Libya and Egypt southward (Figure 9a) into the African continent, before taking an east-to-west trajectory back into the TA within the Harmattan's (see next sections).

[60] The two "northern" outbreaks in Figure 9a (comma shaped streaklines above 40°N) correspond to pollution vented into the middle and upper troposphere by moist convection. The easternmost plume was first vented up to 8000 m MSL by moist convection over northern Italy and then transported eastward into the Asian continent under stronger winds: the cross section of the London tracer in Figure 10b can illustrate the height of this type of transport. The second outbreak in Figure 9a (Mediterranean tracer over central Europe) corresponds to a fresh fraction which

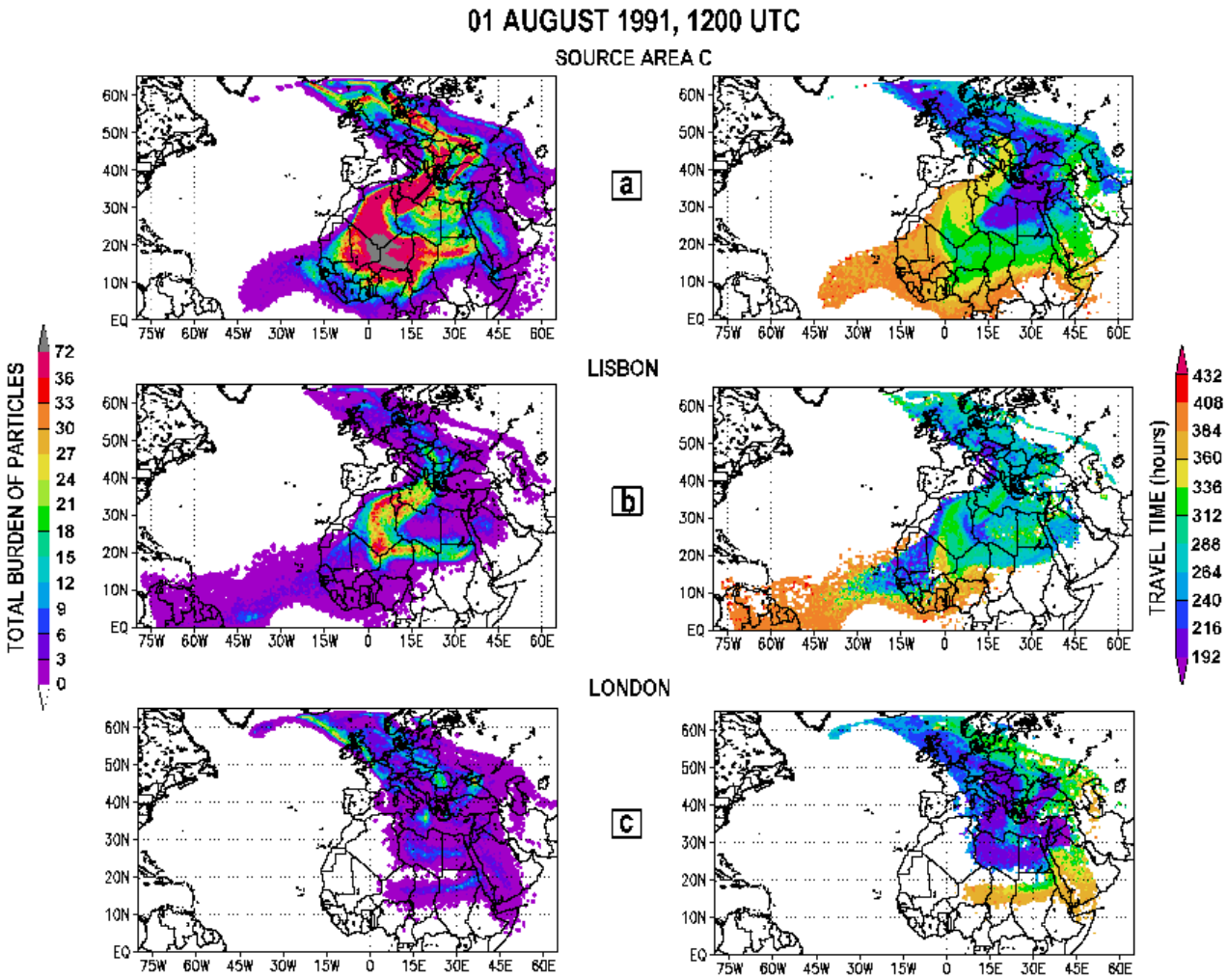

Figure 11. (a–c) Same as Figure 9 but 17 days after tracer release initiation.

will also travel rapidly to the Asian continent between latitudes 50–60°N, after a small perturbation associated with a frontal system crossing the Atlantic coast of France on 23 July. Similar trajectories were simulated for source region D (southwestern Mediterranean, not shown). Analogous comma shape streaklines are observed for the northern emissions (see the London tracer in Figure 9c) as a result of the same atmospheric processes. Their main transport pathways cross central Europe toward Asia, while a smaller fraction can enter the Mediterranean at lower levels. As described above, the height of the transport to Asia is observed in Figure 10b.

[61] Direct pathways into the Mediterranean for the London tracer occur at lower levels (up to 2000 m MSL), mainly along the Bosporus and Dardanelles straits, forced by the Etesian winds at the eastern Mediterranean (Figures 9c and 10b between 32 and 35°N), with a smaller fraction forced by the Tramontana and Mistral winds into the Gulf of Lyon at the WMB [*Gangoiti et al.*, 2001], as shown in Figure 9c. Similar pathways are simulated for the rest of emissions from the northern sources (region A). The emissions from source region B behave like those from the Mediterranean (regions C and D) with small differences, with the exceptions of the A Coruña and Lisbon tracers, discussed above.

4.3.2. Seventeen Days After the Initial Release Time: Transport in Northern Africa and the Mediterranean Under Perturbed Conditions, First Outbreaks Into the Tropical Atlantic

[62] The tracer release is already finished at the source regions, and the perturbation affecting northern Africa and the Mediterranean basin, initiated on 29 July at the Atlantic coast of Africa is now fading there, while propagating along the Mediterranean (Figures 11a and 11b). All the tracers from source regions B and D show slightly similar streaklines to those from region C in Figure 11a, except for the Lisbon (Figure 11b) and A Coruña (not shown) sources. For all of them transport into the TA is first directed to the Mediterranean and then to northern Africa, crossing the coasts of Tunisia and Libya, while the tracers from the western coast of Iberia have an alternative and shorter pathway into the TA.

[63] The consequences of the perturbed meteorology over northwestern Africa can be seen in Figures 11a and 11b: above latitude 20°N over the western coast of Africa, fresh and aged European tracers from source regions B, C and D,

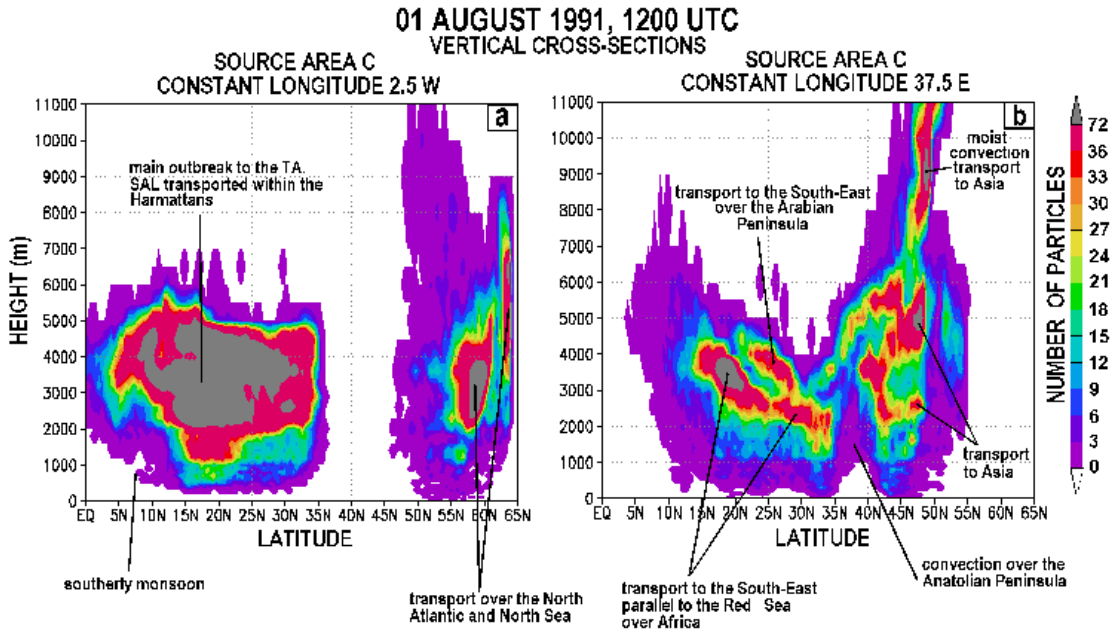

Figure 12. (a) Vertical cross section, centered at constant longitude 2.5°W (10°W–5°E), corresponding to the western boundary of the main plume front, from source area C in Figure 11a. (b) Vertical cross section centered at longitude 37.5°E (30–45°E) (eastern boundary) of the same plume.

some of them recirculating over the Atlas mountains, are now pushed to the east over central and southern Algeria. Output to the TA is blocked at those latitudes. At the same time the perturbation sweeps the Mediterranean and the plume front is observed over the coast of Libya, the Balkans and eastern Europe. Except for the Lisbon and A Coruña tracers that begin crossing the TA on 21 July, after traveling southward along the coast of west Africa (shortcut), the rest of the European tracers (from regions B, C and D) begin their westward journey off the coast of Africa on 27–28 July, below latitude 20°N, while the massive outbreak to the TA is delayed up to the 4–5 August because of the perturbed meteorology over northern Africa: the main plume front is over Mali in Figures 11a and 11b (1 August) and the same plume front is in the middle of the TA on 10 August (Figure 13a and 13b).

[64] The vertical distribution of the tracer over Africa before crossing to the TA is shown in Figure 12a (a cross section of the Mediterranean tracer in Figure 11a, centered at longitude 2.5°W): The southern plume corresponds to the main outbreak into the TA, with most of the tracer traveling at a well-mixed and elevated layer (the SAL, between 2000 and 5000 m) within the warm and dry Harmattans. Below latitude 15°N the cool and moist southwestern monsoon intrusion into the African continent uplifts the base of the SAL to 3000 m. The tracer over the North Atlantic and North Sea (northern plume in Figure 12a), above latitude 55°N, was released on the 23rd, after the frontal passage over France (Figure 9), and was then vented to the middle and upper troposphere, and transported eastward (not shown) and back again westward, forced by the Anticyclone reinforced over the Scandinavian Peninsula on 28 July, as described in section 2.

[65] Vertical distribution of the Mediterranean tracer at the eastern boundaries of the domain is observed in Figure 12b (a cross section at the same longitudinal position as in Figure 10b). Most of the Mediterranean tracer is transported at elevated layers (above 2000 m MSL). Below latitude 35°N, in the cross section, the plume travels to the southeast, almost parallel to the Red Sea, and is progressively uplifted from 2000 m to 4000 m (Figure 10b): the stronger uplift, observed at latitude 20°N, corresponds to the position of the northern boundaries of the ITF at eastern Africa. Above this plume, and between latitudes 20–30°N, the tracer crossing the Arabian Peninsula parallel to the Red Sea is vented at higher altitude (3000–5000 m) by stronger convective activity over the area. The Anatolian Peninsula separates the described southern plume from the northern one, which travels eastward into the Asian continent at a higher altitude, after being vented to the middle and upper troposphere by moist convection. Sinking over the Black Sea and the eastern Mediterranean can draw a fraction of these eastward traveling emissions to lower levels, as shown between latitudes 41–45°N and 31–35°N in Figure 12b.

[66] Emissions from region A (represented by the London tracer in the Figure 11c) have not reached the TA at this time. Only a small fraction of this source region is observed over Africa with the same vertical distribution as that observed for the Mediterranean tracer over the area. According to the tracer age (Figure 11c), two main outbreaks are transported into the African continent across the eastern Mediterranean, in two consecutive intervals showing latitudinal stratification.

4.3.3. Twenty-Six Days After the Initial Release Time: Characteristics of the Transport Over the Tropical Atlantic Into America

[67] Normal conditions now prevail in northern Africa, and tracers from all source regions, except London (Figure 13c) and Cardiff (not shown) have reached the American continent. As already shown, the irruption from

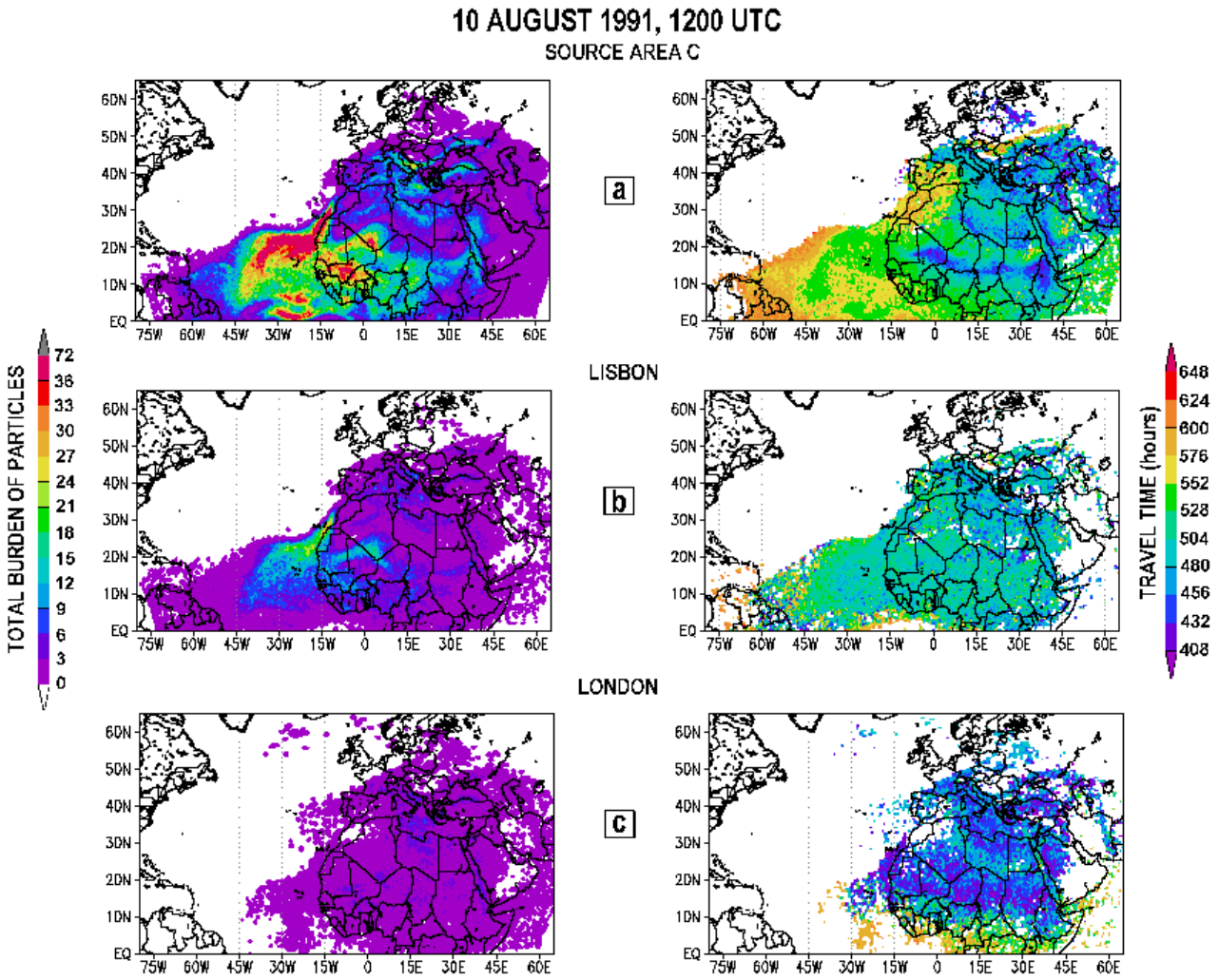

Figure 13. Same as Figures 9 and 11 but 26 days after the tracer release initiation.

western Africa into the TA is far from continuous: an important outbreak of the European tracers off the western coast of Africa took place on 4–5 August (not shown), after the massive turn around northeastern Africa during the perturbed period. Figure 13 shows the main plume front of this outbreak over the central TA, following 5–6 days of travel over the ocean. Sources from region A do not contribute significantly to the tracer concentration over the TA, but, as shown in Figure 13c, they can also be detected traveling westward to America.

[68] The main outbreak over the ocean, above latitude 15°N (Figures 13a and 13b), takes place under strong wind shear between the SAL, transporting the main fraction of the plume, and the marine layer, which is topped by the trade wind inversion. Below latitude 16–17°N, the southwestern monsoon creates a large area of instability, which is clearly observed inland in Figure 14a between latitudes 4–16°N. The cross section in Figure 14a is at the same place as the one in Figure 12a, but at this time moist convection is present and powerful updrafts and downdrafts vent the SAL to the upper troposphere and bring a fraction to the lower levels (1500–4000 m MSL in Figure 14a) over land. Simultaneously, a general uplift of the SAL base is observed, up to 5000 m MSL, associated with the cooler monsoon inland advection.

[69] Between latitudes 37–40°N in Figure 14a, a deep injection of the Mediterranean tracer to the upper troposphere is observed after a perturbation over eastern Iberia, which entered the western Mediterranean on 9 August and moved to the central Mediterranean on 11 August. As discussed in section 4.1, diurnal cycles in the WMB were affected, but the circulation over northern Africa did not show any important changes.

[70] The main characteristics of the European plume transport over the Atlantic Ocean toward America can be observed in a cross section at constant latitude: Figure 14b shows the longitudinal distribution of the tracer from Mediterranean source region C in Figure 13a. The section is centered at latitude 15°N and represents the total number of particles between latitudes 10°N and 20°N. These latitudes correspond to the main Atlantic corridor for both European pollution and Saharan dust [*Karyampudi et al.*, 1999]. The main plume from the Mediterranean region is observed at the SAL (between

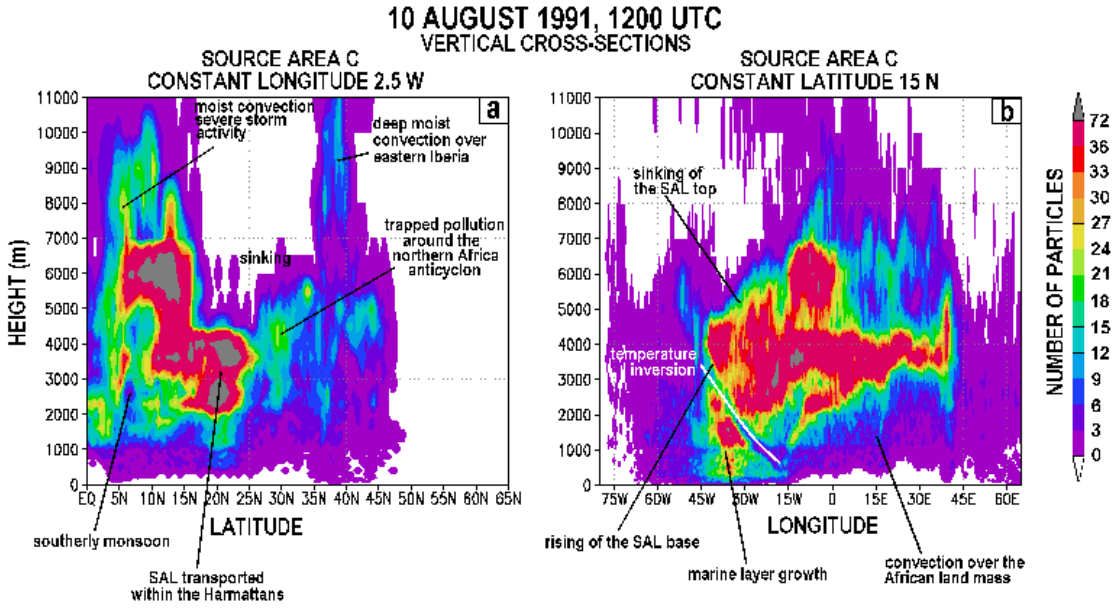

Figure 14. (a) Vertical cross section of the plume from source area C in Figure 13a and at the same place as in Figure 12a, showing plume vertical distribution over Africa before crossing to the TA. (b) Vertical cross section, centered at constant latitude 15°N (10–20°N), corresponding to the latitudes of the main Atlantic transport. Evolution of the air mass in its progress to America is shown.

2000 and 6000 m MSL), before crossing the western coast of Africa (longitude 15°W in Figure 14b). The sinking of the tracer top within the SAL and the rising of its base are clearly shown as the plume travels over the TA (longitudes 15–40°W). Both processes have already been incorporated in *Karyampudi et al.*'s [1999] dust plume conceptual model.

[71] The cooler marine air layer, with an initial depth of 500–1000 m at western Africa (longitude 15°W in Figure 14b), shows continuous growth up to 2500 m at longitude 40°W, after traveling 2700 km over the ocean. Both the marine layer and the SAL are visible in the tracer concentration distribution, clearly separated by a temperature inversion rising from east to west (trade wind inversion) and containing very low tracer concentrations near the coast of Africa. The concentration in the marine layer increases westward at the same time that it deepens. The explanation of these processes remains controversial [*Reid et al.*, 2003] but, after analyzing the meteorological evolution of both the SAL and the marine layer over the TA, we conclude that the sinking of the SAL top results from the generalized air mass sinking within the Atlantic high-pressure system, and the rise of the SAL base (rise of the trade wind inversion) is caused by convection over an increasing east-to-west SST. Westward trade winds traveling in the marine layer transport the excess heat from the sea surface to the upper levels, resulting in the observed deepening of the marine layer and mixing within the trades. During its westward evolution, convection within the trades entrains tracer material from the SAL base into the marine layer (the simulation shows a high tracer concentration at the top of the marine layer and a decreasing concentration in lower layers), and, at the same time, the temperature inversion is uplifted. Once entrained in the marine layer during the oceanic transport, wind shear

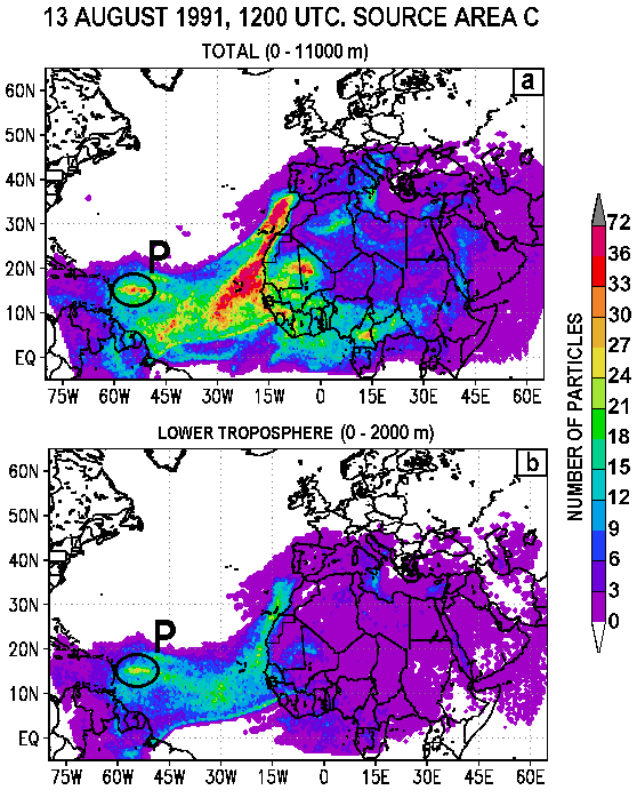

Figure 15. Particle burden of the tracer from source area C, 29 days after the initial release (a) for the total atmospheric column and (b) for the lower 2000 m. Particle cloud P corresponds to a lower-level intrusion to the Caribbean after being entrained from the SAL layer at the middle of the TA.

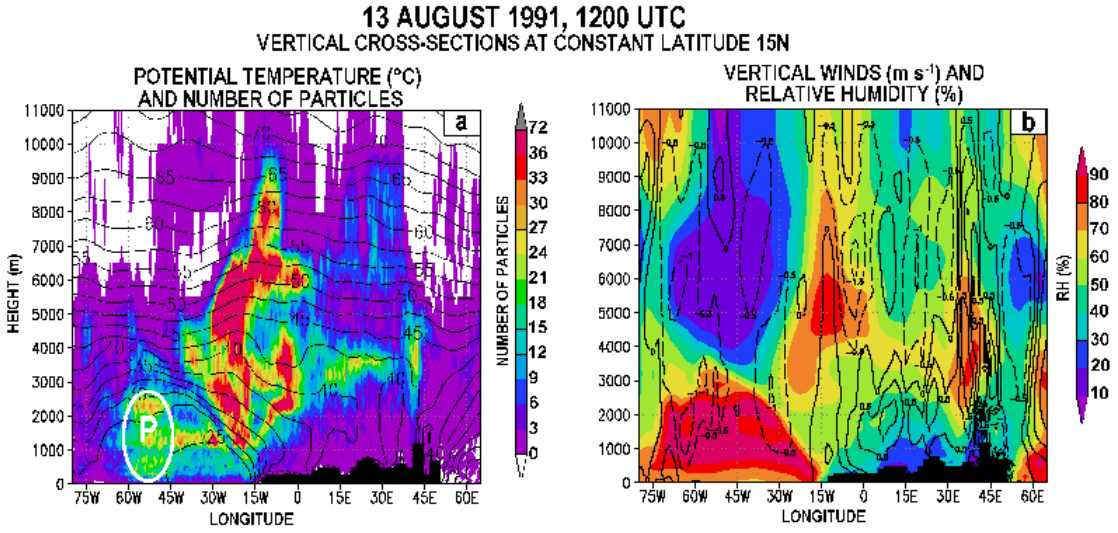

Figure 16. (a) Vertical cross section of the plume from source area C in Figure 15a (represented in shaded colors), centered at constant latitude 15°N (10–20°N), same as Figure 14b, and average potential temperature in contour lines. The cloud of particles marked P is the same as in Figures 15a and 15b. (b) Relative humidity (shaded colors) and vertical winds (in contour lines) for the same cross section: solid line is for positive-upward and dashed line is for negative-downward. The terrain profile is included at the bottom.

between both layers can transport the tracer to different locations and at different rates within the Caribbean.

4.3.4. Twenty-Nine Days After the Initial Release Time: Arrival at the Caribbean

[72] Figures 15 and 16 substantiate the meteorological mechanisms operating during this oceanic transport. The massive Mediterranean tracer front observed in Figure 13a over the middle of the TA is now (3 days later) over the Caribbean and coastal areas of South America (Figure 15a). Figure 15b shows the consequences of the entrainment of the SAL tracer in the marine layer (only concentrations for the lowest 2000 m of the atmosphere are depicted). The northwestern coast of Africa (still recirculating pollutants around the Atlas) draws a fraction of the tracer into lower levels (1000–2000 m) in the coastal convective cells and associated enhanced compensatory sinking over the coastal cooler waters: the long streak line at western Africa between 20°N and 35°N in Figure 15b is a consequence of this process.

[73] At the western TA, the plume crossing to the Caribbean in Figure 15 (marked P), was mainly transported at lower levels (marine layer) after entrainment from the SAL during the transoceanic transport. However, the fraction arriving over the coastal areas of South America (Figure 15a) is being transported at higher levels (4000–7000 m). This latitudinal segregation of the tracer may not be the rule for the transport process: the onset of southeasterly winds at 700 hPa on the following days could transport the European tracer at both the SAL and the marine layer over the Caribbean.

[74] There is general consistency between the arrival of the European tracer at the Caribbean and the data from the University of Miami surface stations (Barbados and Miami). Barbados daily data (not shown) recorded modest dust concentrations (2 $\mu g\ m^{-3}$) and low levels of NO_3^- (0.19 $\mu g\ m^{-3}$) and non-sea-salt (nss) $SO_4^=$ (0.42 $\mu g\ m^{-3}$) on 10–11 August. However, on the following days, the concentrations jump sharply reaching peak levels of dust (100 $\mu g\ m^{-3}$), nss sulfate (1.88 $\mu g\ m^{-3}$) and a lower nitrate peak (0.69 $\mu g\ m^{-3}$) on 13 August: the sulfate-nitrate peaks coincide with the dust peaks, and concentrations are higher than those normally associated with unimpacted ocean regions [*Savoie et al.*, 2002; *Prospero*, 1999]. This is consistent with Figure 15, which shows an intrusion over the region on 13 August. The Miami record on 17 August shows sharp peak concentrations of nitrate and nss sulfate (6.1 and 6.5 $\mu g\ m^{-3}$, respectively): the highest values of the summer. This is also consistent with the movement of the tracer in Figure 15, which shows the plume arcing to the north on its way to Miami, in a "usual" transport pathway for joint dust and sulfate-nitrate episodes in Florida [*Prospero*, 1999].

[75] The cross section at constant latitude in Figure 16a shows the longitudinal distribution of the Mediterranean tracer (region C) observed in Figure 15. As in Figure 14b, the cross section is centered at latitude 15°N, and represents the total number of particles between latitudes 10°N and 20°N. Modeled potential temperature is also represented in contour levels. The relative humidity (shaded colors) and the wind vertical velocity (contour lines) are represented in Figure 16b for the same cross section. Again, the sinking of the SAL top and the westward rise of its base are clearly observed over a developing marine layer. The temperature inversion at 500–1000 m over western Africa (15°W, in Figure 16a) is lifted to 2500 m near the Caribbean: the progressive mixing of the marine layer, as it flows westward over an increasing SST, causes it to deepen and entrain pollutants from the SAL. Thus a mixed marine layer (almost constant potential temperature distribution with height) arrives at the western TA.

[76] The fraction of tracer traveling at greater heights within the SAL and above the trade wind inversion in Figure 16a (longitude 40°W, 3500–4500 m MSL) crosses to lower latitudes in the middle of the TA (longitude 40°W) and disappears from the cross section (its continuity is observed entering the eastern coast of South America in Figure 15a).

[77] The relative humidity and vertical wind velocity distribution in the marine layer and SAL in Figure 16b confirms our flow description: (1) dry air masses sinking over the whole TA (15–65°W in Figure 16b), associated with Atlantic high-pressure system dynamics affecting the SAL; (2) suppressed sinking near the top of the marine layer (highest relative humidity); and (3) almost-saturated marine layer at the western coast of Africa (low SST), while its relative humidity decreases east to west to 70% after heating over a progressively higher SST from east to west.

[78] The simulated meteorological processes work not only for our passive tracer, but also for the dust transport into the Caribbean. Our simulated vertical layering is consistent with the aircraft measurements during the Barbados Oceanographic and Meteorological Experiment (BOMEX) [*Prospero and Carlson*, 1972] and the more recent Puerto Rico Dust Experiment (PRIDE) [*Reid et al.*, 2002; *Reid et al.*, 2003; *Maring et al.*, 2003]. The latter has shown complex vertical layering of the African soil dust arriving at the Caribbean, and does not correspond to the commonly assumed SAL transport dynamics: during the 26 days of the experiment from mid-June to July 2000, dust was found at the SAL (typical dust transport during the summer) above the trade inversion, at the marine layer, or at both layers. This is consistent with the transport dynamics shown in our simulations and described in the previous paragraphs. This described dynamics enables the joint dust and European pollution to be transported in both layers and enter the Caribbean decoupled from each other.

[79] Convection at the top of the marine layer associated with fair weather cumulus clouds (the convective boundary layer, between the marine layer and the trade inversion), as described by *Reid et al.* [2003], could be playing a role in the entrainment of dust from the SAL into the marine layer. These clouds cover large areas of the Atlantic Ocean underneath the SAL transport pathway, but the entrainment does not need clouds to happen. Upward transport of sensible flux from an increasing SST from east to west could produce a similar result, although the moist convection could be more efficient. We can now speculate about the efficiency of these and other possible entrainment mechanisms and their relation to the actual depth of the marine layer (1800–2300 m MSL, during the PRIDE experiment), but this approach needs further research (experimental field programs and modeling).

[80] Besides the TA transport processes, large dry convection areas are observed at lower levels over land in the African continent (Figures 16a and 16b), with upward wind velocities and low relative humidity. Mixing and convection result in the formation of a boundary layer with an almost constant potential temperature from the surface up to 4000–5000 m over continental areas of Africa (Figure 16a). Above this mixing layer, sinking is observed over the African continent, associated with the high-pressure system in the upper levels above northern Africa. Thus the main tracer plume at the SAL accumulates at the top of the mixing layer and it is trapped at the bottom of the sinking motion. Moist deep convection is also frequently present at these latitudes over the landmass: a developing convective system is depicted between 35 and 45°E in Figure 16; it will vent the tracer to the upper troposphere at the eastern coast of Africa. Another convective system is dissipating over the western coast (between longitudes 0–15°W in Figure 16), and the tracer is observed up to the 10,000 m height after being vented from the SAL.

Table 1. Percentage of the Tracer Transported Into America Across the Tropical Atlantic

Source Region	Town	Percentage
A	London	17.4
A	Cardiff	18.6
A	Le Havre	25.7
A	Paris	25
B	Bordeaux	61.7
B	Bilbao	51.2
B	A Coruña	71.4
B	Lisbon	77.7
B	Madrid	60.9
C	Lyon	46.2
C	Toulouse	61.4
C	Marseille	63
C	Barcelona	62.7
D	Tarragona	60.6
D	Valencia	60.7
D	Palma	56.9
D	Cartagena	65.5

[81] We can now quantify the contributions of this trans-Atlantic transport into the American continent following either of the described mechanisms. Table 1 summarizes the relative percentage of tracer transported to the American continent (crossing the 60°E longitude westward) over the total emitted at the source: more than 50% of the emissions from source regions B, C and D reach the American coasts after traveling over the Mediterranean and northern Africa. This is by far the preferred pathway and it is also significant for region A. The highest percentages, observed for Lisbon and A Coruña in western Iberia, result from their ability to shift between two alternative pathways: the Atlantic shortcut and the (longer) Mediterranean pathway. It is important to note that no removal mechanisms were incorporated in our simulations (with the exception of particle loss across domain boundaries). Thus the estimated transport should be reduced accordingly.

[82] As shown in Table 1, all sources, except the northern emissions (region A), contribute a similar fraction to the transport, with a rather small standard deviation. This exceptional behavior might have meaning in terms of the atmospheric selection of preferred pathways. The mean synoptic scenario shown in Figure 2, and other similar ones, which can be produced by averaging from June to September (not shown), reveals quasi-steady flow dynamics (low standard deviations below latitudes 30–40°N) and stable conditions (associated with sinking above the trade inversion) for the air masses involved in the ICT transport from the Mediterranean and northern Africa to the Caribbean. The Atlantic anticyclone and its extension to northern Africa (a persistent feature above the mixing layer over the African landmass during the warm season) are responsible

for the observed efficiency in the ICT transport of European pollution and dust: dry convection within the mixing layer over northern Africa contributes to the accumulation and layering of dust and pollutants (reservoir layers) in the middle troposphere (SAL formation over Africa: Figure 12a). Sinking also prevails at these levels above the trades during the oceanic transport, and adds to the stability of the reservoir layers in their transport to America (Figures 14 and 16): thus the SAL becomes less dispersive as it crosses the Atlantic Ocean and contributes to the formation of thin dust pollution layers that expand hundreds of kilometers, as observed during the PRIDE experiment [*Reid et al.*, 2003].

5. Summary and Conclusions

[83] A modeling system based on the mesoscale model RAMS coupled with the dispersion model HYPACT has been used to reproduce the regional-scale meteorology and transport dynamics that led to the WMB ozone accumulation observed during the flight campaign of the European project RECAPMA (16–19 July 1991). After a further extended and continuous simulation of 32 days (15 July to 16 August 1991), we were also able to reproduce, at the regional-to-continental scale, the main dust circulations over northern Africa and the Mediterranean region observed by TOMS. With these ozone and dust circulations we were able to validate the simulation over different subregions of a larger domain. Our results show that these subdomains are coupled and act together in the export of European pollution and dust, at the intercontinental scale, from the Mediterranean region into the TA and America during the warm season. Thus the flow dynamic described represents regional meteorological scenarios from June to September; for the rest of the year the transport dynamics in the region changes according to the evolution of the large-scale circulation systems [*Prospero and Carlson*, 1972; *Chiapello et al.*, 1995; *Prospero*, 1996].

[84] Excepting a fraction of the emissions from the Atlantic coast of Iberia (Lisbon and A Coruña in our simulations), which can take a full-Atlantic shortcut to the American coasts, most emissions enter the Mediterranean basin and cross into the TA following a longer pathway. This longer pathway for European pollutants (with source regions B, C and D contributing more than 50% of their emissions to the Caribbean) is initially directed eastward to the Mediterranean basin, then crosses the southern coast of the Mediterranean to the North African landmass and finally traverses westward to the west African coast and the TA at elevated layers, between 2000 and 6000 m MSL (the Saharan air layer (SAL)). Once the European pollution reaches the TA it is transported over the ocean within the trade winds to the American coasts in a travel time of around 8 days. Quantification of the relative contribution of European sources to TA transport to America (Table 1) is mainly limited by the assumptions made in our dispersion simulation approach: passive tracer, source simplifications and, most importantly, no removal mechanisms. This should be taken into account for interpreting the results in Table 1, which can be considered a sort of ''transport dynamical efficiency.''

[85] During transit across the Mediterranean and over the African continent, an important fraction of the pollutants (and dust) recirculates within the semipermanent high-pressure system located aloft over northern Africa during the warm season. This anticyclonic circulation, above the 700 hPa pressure level, is a key feature of the circulatory complex controlling the export and redistribution of dust and European pollution within the SAL. The joint dust and pollution plume can be forced to turn around the southwestern Atlas back to the Iberian Peninsula and the western Mediterranean, instead of crossing directly to the TA. This causes aging of the air mass, accumulation over the area and a delay in the transport off the western coast of Africa.

[86] Depending on the weather regime over northern Africa, it will take 20–26 days for the emissions from regions B, C and D to reach American coasts (longitude 60°W): the shorter travel times for normal conditions and longer travel times for perturbed conditions. This estimation is at least 1 week longer than the evaluation of *Hamelin et al.* [1989]. The longest travel time to reach American coasts corresponds to emissions from source region A, which takes up to 28 days. This travel time is closer to the estimations by *Stohl et al.* [2002] for the ''secondary plume'' observed over the TA at 15°N, in their simulations of the summer transport of European CO emissions. In contrast, the shorter travel times correspond to the fraction of emissions from western Iberia which, under favorable conditions, take no more than 11–12 days, an estimate more in agreement with previous evaluations by *Hamelin et al.* [1989]. Other possible pathways, such as the venting of the Mediterranean MBL through Gibraltar, will likely follow processes similar to those described for the emissions from the Iberian western coast.

[87] The vertical distribution of the mixed Saharan dust and European pollution plume changes along the trajectory, controlled by the atmospheric dynamics at each location:

[88] 1. Daytime dry convection over the arid landmass of northern Africa is the mechanism for uplifting European pollution into the SAL. Simultaneous sinking at higher levels (above 4000 m MSL) over large continental areas within the North African anticyclone, mainly above latitude 15°N, traps the pollutants at elevated layers (2000–5000 m) and precludes their venting to the upper troposphere. Major outbreaks from western Africa into the TA initiate the oceanic trip at those levels. Exceptionally, higher heights can be reached after up-slope daytime venting at the southern flanks of the Atlas Mountains: dust and pollutants can be injected up to 6000–7000 m MSL, in agreement with LIDAR observations by *Karyampudi et al.* [1999].

[89] 2. Below latitude 15°N, moist convection mechanisms for the vertical venting of the dust and pollution are more likely. They can reach the upper troposphere and/or be rain-scavenged in the ITF storm belt. Our simulations show that at these lower latitudes westward transport occurs at higher levels than at latitudes above 15°N.

[90] Once the pollutants are exported to the TA, the sinking of the SAL top and the rising of its base are clearly shown in our model results. These processes have been previously documented by other authors (see section 4.3) but their explanation is still under discussion. HYPACT simulations also show a westward increase in tracer concentration within the marine layer. Our analysis shows that the sinking of the SAL top results from the generalized air mass sinking within the Atlantic high-pressure system, and

the rising of the SAL base is caused by convection within the marine layer over increasing SSTs from east to west. Convection entrains tracer material from the SAL base into the marine layer and the temperature inversion is uplifted during the transit over the TA. Once entrained in the marine layer, wind shear between both layers can transport the tracer to different locations within the Caribbean. These mechanisms can provide new perspectives on the dust layering and thermal and humidity stratifications observed over the Caribbean during past experiments (section 4.3). A general consistency is also observed between the arrival of the pollution tracer fronts at the Caribbean and the nss sulfate and nitrate episodes recorded at the University of Miami surface stations (Barbados and Miami).

[91] There are still important questions to be answered in relation to transport dynamics (section 4.3), removal efficiencies and a more accurate quantification and identification of transported species. The implications of these revealed links between the export of pollutants from Europe across the Mediterranean and northern Africa, and the dust and pollution episodes in the Caribbean can affect a wide range of scientific issues: sulfatation and nitrification of Saharan dust, fertilization of the African rain forest, the Amazon basin and the TA ocean, perturbations in the hydrological cycle as well as perturbations to the extratropical depressions and tropical cyclone activity, among others.

[92] **Acknowledgments.** The experimental data and part of the modeling results used here were obtained under the European Commission project RECAPMA (Regional Cycles of Air Pollution in the Western Mediterranean Area, 1990–1992). The Commisariat à l'Energie Atomique (CEA), Saclay, France, supported the RECAPMA flights. Additional financing was provided by the National Research Program of the Spanish Ministry of Science and Technology, Project TRAMA (Characterization of the Pollution TRAnsport Mechanisms between the Western Mediterranean Basin and the Atlantic Ocean, CGL2004-04448). The authors would like to thank Joseph Prospero of the University of Miami, CIMAS, for his insightful input and assistance with the interpretation of the Barbados-Miami records.

References

Chen, C., and W. R. Cotton (1983), A one-dimensional simulation of the stratocumulus-capped mixed layer, *Boundary Layer Meteorol.*, *25*, 289–321.

Chiapello, I., G. Bergametti, F. Dulac, L. Gomes, B. Chatenet, J. Pimenta, and E. S. Suares (1995), An additional low layer transport of Sahelian and Saharan dust over the northeastern tropical Atlantic, *Geophys. Res. Lett.*, *22*, 3191–3194.

Chiapello, I., J. M. Prospero, J. R. Herman, and N. C. Hsu (1999), Detection of mineral dust over the North Atlantic Ocean and Africa with the Nimbus 7 TOMS, *J. Geophys. Res.*, *104*, 9277–9292.

Duncan, B. N., and I. Bey (2004), A modeling study of the export pathways of pollution from Europe: Seasonal and interannual variations (1987–1997), *J. Geophys. Res.*, *109*, D08301, doi:10.1029/2003JD004079.

Falkowski, P. G., R. T. Barber, and V. Smetacek (1998), Biogeochemical controls and feedbacks on ocean primary production, *Science*, *281*, 200–206.

Fehsenfeld, F. C., P. Daum, W. R. Leaitch, M. Trainer, D. D. Parrish, and D. Hübler (1996), Transport and processing of O3 and O3 precursors over the North Atlantic: An overview of the 1993 North Atlantic Regional Experiment (NARE) summer intensive, *J. Geophys. Res.*, *101*, 28,877–28,891.

Fortezza, F., V. Strocchi, G. Ciovanelli, P. Bonasoni, and T. Georgiadis (1993), Transport of photochemical oxidants along the northwestern Adriatic Coast, *Atmos. Environ., Part A*, *27*, 2393–2402.

Gangoiti, G., M. M. Millán, R. Salvador, and E. Mantilla (2001), Long-range transport and re-circulation of pollutants in the western Mediterranean during the RECAPMA Project, *Atmos. Environ.*, *35*, 6267–6276.

Georgiadis, T., G. Giovanelli, and F. Fortezza (1994), Vertical layering of photochemical ozone during land-sea breeze transport, *Nuovo Cimento*, *17*, 371–375.

Giannini, A., R. Saravanan, and P. Chang (2003), Oceanic forcing of Sahel rainfall on interannual to interdecadal time scales, *Science*, *302*, 1027–1030.

Hamelin, B., F. E. Grousset, P. E. Biscaye, A. Zindler, and J. M. Prospero (1989), Lead isotopes in trade wind aerosols at Barbados: The influence of European emissions over the North Atlantic, *J. Geophys. Res.*, *94*, 16,243–16,250.

Helfand, H. M., and J. C. Labraga (1988), Design of a nonsingular level 2.5 second-order closure model for the prediction of atmospheric turbulence, *J. Atmos. Sci.*, *45*, 113–132.

Herman, J. R., P. K. Bhartia, O. Torres, N. C. Hsu, C. J. Seftor, and E. Celarier (1997), Global distribution of UV-absorbing aerosols from Nimbus 7/TOMS data, *J. Geophys. Res.*, *102*, 16,911–16,922.

Hoell, J. M., D. D. Davis, S. C. Liu, R. E. Newell, H. Akimoto, R. McNeal, and R. J. Bendura (1997), The Pacific Exploratory Mission West Phase B: February–March, 1994, *J. Geophys. Res.*, *102*, 28,223–28,239.

Iversen, T. (1984), On the atmospheric transport of pollution to the Arctic, *Geophys. Res. Lett.*, *11*, 457–460.

Jacob, D. J., J. H. Crawford, M. M. Kleb, V. S. Connors, R. J. Bendura, J. L. Raper, G. W. Sachse, J. C. Gille, L. Emmons, and C. L. Heald (2003), The transport and chemical evolution over the Pacific (TRACE-P) aircraft mission: Design, execution, and first results, *J. Geophys. Res.*, *108*(D20), 9000, doi:10.1029/2002JD003276.

Jickells, T. D., et al. (2005), Global iron connections between desert dust, ocean biogeochemistry, and climate, *Science*, *308*, 67–71.

Kallos, G. (Ed.) (1997), Transport and transformation of air pollutants from Europe to the east Mediterranean region (T-TRAPEM), *Final Rep. Contract AVI-CT92-0005*, Eur. Comm., Brussels.

Kallos, G., P. Kassomenos, and R. A. Pielke (1993), Synoptic and mesoscale weather conditions during air pollution episodes in Athens, Greece, *Boundary Layer Meteorol.*, *62*, 163–184.

Kallos, G., V. Kotroni, K. Lagouvardos, and A. Papadopoulos (1998), On the long-range transport of air pollutants from Europe to Africa, *Geophys. Res. Lett.*, *25*(5), 619–622.

Karyampudi, V. M., et al. (1999), Validation of the Saharan dust plume conceptual model using Lidar, Meteosat, and ECMWF data, *Bull. Am. Meteorol. Soc.*, *80*, 1045–1075.

Lamarque, J.-F., and P. G. Hess (2003), Model analysis of the temporal and geographical origin of the CO distribution during the TOPSE campaign, *J. Geophys. Res.*, *108*(D4), 8354, doi:10.1029/2002JD002077.

Lamb, P. J., and R. A. Peppler (1992), Further case studies of tropical Atlantic surface atmospheric and oceanic patterns associated with Subsaharan drought, *J. Clim.*, *5*, 476–488.

Lelieveld, J., et al. (2002), Global air pollution crossroads over the Mediterranean, *Science*, *298*, 794–799.

Luria, M., M. Peleg, G. Sharf, D. A. Siman-Tov, N. Schpitz, Y. B. Ami, Z. Gawi, B. Lifischitz, A. Yitzchaki, and I. Seter (1996), Atmospheric sulphur over the East Mediterranean region, *J. Geophys. Res.*, *101*, 25,917–25,930.

Maring, H., D. L. Savioe, M. A. Izaguirre, L. Custals, and J. S. Reid (2003), Vertical distributions of dust and sea-salt aerosols over Puerto Rico during PRIDE measured from a light aircraft, *J. Geophys. Res.*, *108*(D19), 8587, doi:10.1029/2002JD002544.

McKendry, I. G., J. P. Hacker, R. Stull, S. Sakiyama, D. Mignacca, and K. Reid (2001), Long-range transport of Asian dust to the Lower Fraser Valley, British Columbia, Canada, *J. Geophys. Res.*, *106*, 18,361–18,370.

Mellor, G. L., and T. Yamada (1982), Development of a turbulence closure model for geophysical fluid problems, *Rev. Geophys.*, *20*, 851–875.

Michaels, A. F., D. Olson, J. Sarmiento, J. Ammerman, K. Fanning, R. Jahnke, A. H. Knap, F. Lipschultz, and J. Prospero (1996), Inputs, losses and transformations of nitrogen and phosphorus in the pelagic North Atlantic Ocean, *Biogeochemistry*, *35*, 181–226.

Millán, M. M., B. Artíñano, L. Alonso, M. Castro, R. Fernandez-Patier, and J. Goberna (1992), MEso-meteorological Cycles of Air Pollution in the Iberian Peninsula, (MECAPIP), *Contract EV4V-0097-E, Air Pollut. Res. Rep. 44*, 219 pp., Eur. Comm., Brussels.

Millán, M. M., R. Salvador, E. Mantilla, and B. Artíñano (1996), Meteorology and photochemical air pollution in southern Europe: Experimental results from EC research projects, *Atmos. Environ.*, *30*, 1909–1924.

Millán, M. M., R. Salvador, E. Mantilla, and G. Kallos (1997), Photooxidant dynamics in the western Mediterranean in summer: Results from European research projects, *J. Geophys. Res.*, *102*(D7), 8811–8823.

Millán, M. M., E. Mantilla, R. Salvador, A. Carratalá, M. J. Sanz, L. Alonso, G. Gangoiti, and M. Navazo (2000), Ozone cycles in the western Mediterranean basin: Interpretation of monitoring data in complex coastal terrain, *J. Appl. Meteorol.*, *39*, 487–508.

Millán, M. M., et al. (2005), Climatic feedbacks and desertification: The Mediterranean model, *J. Clim.*, *18*, 687–701.

Newell, R. E., and M. J. Evans (2000), Seasonal changes in pollutant transport to the North Pacific: The relative importance of Asian and European sources, *Geophys. Res. Lett.*, *27*, 2509–2512.

Nicholson, S. E., B. Some, and B. Kone (2000), An analysis of recent rainfall conditions in West Africa, including the rainy seasons of the 1997 El Niño and the 1998 La Niña years, *J. Clim.*, *13*, 2628–2640.

Orciari, R., T. Georgiadis, F. Fortezza, L. Alberti, G. Leoncini, L. Venieri, V. Gnani, T. Montanari, and E. Rambelli (1998), Vertical evolution of photochemical ozone over greater Ravenna, *Ann. Chim.*, *88*, 403–411.

Pielke, R. A., et al. (1992), A comprehensive meteorological modelling system–RAMS, *Meteorol. Atmos. Phys.*, *49*, 69–91.

Prospero, J. M. (1996), Saharan dust transport over the North Atlantic Ocean and Mediterranean: An overview, in *The Impact of African Dust Across the Mediterranean*, edited by S. Guerzoni and R. Chester, pp. 131–151, Springer, New York.

Prospero, J. M. (1999), Long term measurements of the transport of African mineral dust to the southeastern United States: Implications for regional air quality, *J. Geophys. Res.*, *104*(D13), 15,917–15,927.

Prospero, J. M., and T. N. Carlson (1972), Vertical and areal distribution of Saharan dust over the western equatorial North Atlantic Ocean, *J. Geophys. Res.*, *77*, 5255–5265.

Prospero, J. M., and P. J. Lamb (2003), African droughts and dust transport to the Caribbean: Climate change implications, *Science*, *302*, 1024–1027.

Prospero, J. M., P. Ginoux, O. Torres, S. E. Nicholson, and T. E. Gill (2002), Environmental characterization of global sources of atmospheric soil dust identified with the Nimbus 7 total ozone mapping spectrometer (TOMS) absorbing aerosol product, *Rev. Geophys.*, *40*(1), 1002, doi:10.1029/2000RG000095.

Rayner, N. A., E. B. Horton, D. E. Parker, C. K. Folland, and R. B. Hackett (1996), Version 2.2 of the global sea-ice and sea surface temperature data set, 1903–1994, *CRTN 74*, Hadley Cent., Met Office, Bracknell, U. K.

Reid, J. S., D. L. Westphal, J. M. Livingston, D. L. Savoie, H. B. Maring, H. H. Jonsson, D. P. Eleuterio, J. E. Kinney, and E. A. Reid (2002), Dust vertical distribution in the Caribbean during the Puerto Rico Dust Experiment, *Geophys. Res. Lett.*, *29*(7), 1151, doi:10.1029/2001GL014092.

Reid, J. S., et al. (2003), Analysis of measurements of Saharan dust by airborne and ground based remote sensing methods during the Puerto Rico Dust Experiment (PRIDE), *J. Geophys. Res.*, *108*(D19), 8586, doi:10.1029/2002JD002493.

Reynolds, R. W., and T. M. Smith (1994), Improved global sea surface temperature analyses using optimum interpolation, *J. Clim.*, *7*, 929–948.

Savoie, D. L., J. M. Prospero, S. J. Oltmans, W. C. Graustein, K. K. Turekian, J. T. Merrill, and H. Levy II (1992), Sources of nitrate and ozone in the marine boundary layer of the tropical North Atlantic, *J. Geophys. Res.*, *97*, 11,575–11,589.

Savoie, D. L., R. Arimoto, W. C. Keene, J. M. Prospero, R. A. Duce, and J. N. Galloway (2002), Marine biogenic and anthropogenic contributions to non-sea-salt sulfate in the marine boundary layer over the North Atlantic Ocean, *J. Geophys. Res.*, *107*(D18), 4356, doi:10.1029/2001JD000970.

Schnell, R. C. (1984), Arctic haze and the Arctic gas and aerosol sampling program (AGASP), *Geophys. Res. Lett.*, *11*, 361–364.

Shipman, M. C., A. S. Bachmeier, D. R. Cahoon Jr., and E. V. Browell (1992), Meteorological overview of the Arctic Boundary Layer Expedition (ABLE 3A) flight series, *J. Geophys. Res.*, *97*, 16,395–16,419.

Stohl, A., S. Eckhardt, C. Forster, P. James, and N. Spichtinger (2002), On the pathways and timescales of intercontinental airpollution transport, *J. Geophys. Res.*, *107*(D23), 4684, doi:10.1029/2001JD001396.

Torres, O., P. K. Bhartia, J. R. Herman, Z. Ahmad, and J. Gleason (1998), Derivation of aerosol properties from satellite measurements of backscattered ultraviolet radiation: Theoretical basis, *J. Geophys. Res.*, *103*, 17,099–17,110.

Tremback, C. J., W. A. Lyons, W. P. Thorson, and R. L. Walko (1993), An emergency response and local weather forecasting software system, in *Proceedings of the 20th ITM on Air Pollution and its Applications*, pp. 423–429, Springer, New York.

Walko, R. L., W. R. Cotton, M. P. Meyers, and J. Y. Harrington (1995), New RAMS cloud microphysics parameterization. Part I: The single-moment scheme, *Atmos. Res.*, *38*, 29–62.

Walko, R. L., et al. (2000), Coupled atmospheric-biophysics-hydrology models for environmental modeling, *J. Appl. Meteorol.*, *39*, 931–944.

Ward, M. N. (1998), Diagnosis and short-lead time prediction of summer rainfall in tropical North Africa and interannual and multi-decadal timescales, *J. Clim.*, *11*, 3167–3191.

Washington, R., M. Todd, N. J. Middleton, and A. S. Goudie (2003), Dust-storm source areas determined by the Total Ozone Monitoring Spectrometer and surface observations, *Ann. Assoc. Am. Geogr.*, *93*(2), 297–313.

Wenig, M., N. Spichtinger, A. Stohl, G. Held, S. Beirle, T. Wagner, B. Jähne, and U. Platt (2003), Intercontinental transport of nitrogen oxide pollution plumes, *Atmos. Chem. Phys.*, *3*, 387–393.

Wilkening, K. E., L. A. Barrie, and M. Engle (2000), Trans-Pacific air pollution, *Science*, *290*, 65–67.

Zeng, N., J. D. Neelin, K.-M. Lau, and C. J. Tucker (1999), Enhancement of interdecadal climate variability in the Sahel by vegetation interaction, *Science*, *286*, 1537–1540.

L. Alonso, G. Gangoiti, J. A. García, and M. Navazo, Escuela Técnica Superior de Ingeniería de Bilbao, Universidad del País Vasco-Euskal Herriko Unibertsitatea, E-48013 Bilbao, Spain. (g.gangoiti@ehu.es)

M. M. Millán, Fundación Centro de Estudios Ambientales del Mediterráneo, Parque Tecnológico, E-46980 Paterna, Valencia, Spain.